Unsteady Aerodynamics of Pitching and Perching Wings

By

Joshua Webb

Thesis

Submitted to the Faculty of the

Graduate School of Vanderbilt University

in partial fulfillment of the requirements

for the degree of

Master of Science

in

Mechanical Engineering

December, 2016

Nashville, Tennessee

Approved:

Haoxiang Luo, Ph.D.

Robert W. Pitz, Ph.D.

Amrutur Anilkumar, Ph.D.

ACKNOWLEDGEMENTS

TABLE OF CONTENTS

LIST OF FIGURES

NOMENCLATURE

U(t)	Time dependent freestream velocity
U_0	Initial freestream velocity
t^*	Non-dimensional time
t	Actual time
T	Total time period to complete pitch-up maneuver
α(t)	Angle of attack as a function of time
ω (t)	Angular velocity as a function of time
Re	Reynolds number
ρ	Density
μ	Viscosity
k	Pitch rate
SC	Pitch rate
a_s	Smoothing parameter
t_1	Start of pitch-up maneuver
t_2	End of pitch-up maneuver
a_0	Maximum angle of pitch-up maneuver
$\dot{\alpha}_0$	Nominal pitch rate
c	Chord length

Chapter I   Introduction

I.1   Aerodynamics of bird wings and applications in UAVs

Birds are very graceful creatures that fly effortless through the air. Mankind has always been fascinated with mimicking this skill; tracing all the way back to 1505 when Leonardo da Vinci was intrigued with human mechanical flight, to the present day's growing interest in micro air vehicles (MAVs). Defense Advanced Research Projects Agency (DARPA) defines MAVs as robotic flyers that have a wingspan under 15 cm. MAVs are a class of miniature unmanned aerial vehicles (UAVs) that have recently taken inspiration from flying insects and birds to achieve unprecedented flight capabilities when comparing against the traditional fixed wing design. This study will treat the terms UAVs and MAVs interchangeably.

There are two common types of UAVs (or better known as drones) that is popular among both consumer commercial markets as well as military applications. With recent advances in microelectronics and wireless communication devices on board, UAVs and/or MAVs have numerous markets and applications which include hobbyist, aerial photography, surveying land, aerial inspections for technical installations that may be difficult, dangerous and costly to access (e.g., bridges, dams, towers, wind mills, etc.), military intelligence, surveillance and reconnaissance missions. The first common type of UAVs is a fixed wing model; these are compact, lightweight units that are capable of fast and efficient forward flights. The second style is a rotary blade based system that can hover and can fly both vertically and horizontally. A third, less common type of UAV is bio-inspired flapping-wing that mimics the natural flight of animals. As their biological counterpart, the flapping-wing UAVs can potentially vary several kinematic parameters that describe the 3D wing motion and thus the aerodynamic forces on each wing. The resultant forces and torques are high relative to the body inertia and may allow the UAVs to perform many kinds of maneuvers in a very short time, e.g., taking off, precision landing, and turning. When both steady flight and unsteady maneuvers are considered, the flapping-wing UAVs are potentially more efficient flight than either of the two aforementioned UAV types in small scale. Pesavento and Wang (2009) documented the first piece of evidence in which unsteady aerodynamics makes a flapping motion less costly than the optimal steady wing motion. More specifically, Pesavento and Wang (2009) found at the scale of insects, a 2-D flapping flight can be more aerodynamically efficient than the optimal fixed wing flight by taking advantage of the interaction of the wing with its wake near wing reversal. That is, the leading-edge vortex generated by the previous stroke had the most significant influence on the succeeding unsteady aerodynamic force. Since the fixed wings and flapping wings have their distinct advantages and are most suitable for different flight modes (i.e., cruise and unsteady maneuvers, respectively), it is conceivable that that in the future, these two propulsion approaches could be combined into one hybrid system for complex missions.

I.2   A brief literature survey

There are generally two research directions in the study of aerodynamics of flapping wings. The first is the direct study of animal's wings by incorporating the animal-specific wing kinematics.

Many experimental and computational studies have been conducted in this direction. Only a few representative cases are listed here for brevity. Experimentally, Dickinson et al (1999) validated that conventional theory on insect flight based solely on translation mechanisms (i.e., delayed stall) could not explain the transient forces generated by hoverfly kinematics. Dickinson et al (1999) stated that there are three distinct mechanisms for insect flight: delayed stall, rotational circulation, and wake capture. Rotational circulation and wake capture both depend on the pronation and supination of the wing during the stroke reversal and are necessary in understanding the rotational mechanisms for unsteady aerodynamics in insect flight. Spedding (2003) investigated the wake structure of a thrust nightingale over a range of natural flight speeds and found that wake structures had enough momentum to provide weight support over the wingbeat. Tobalske et al (2007) found that hummingbirds alter specific wing kinematics (e.g., chord angle, angle of attack, wing beat amplitude, etc.) during forward flight from slow to fast speeds. Hedenstrom and Johansson (2015) documented that bats use a leading-edge vortex and an inverted wing during the upstroke to aid in weight support during hovering and slow speeds. Dudley and Ellington (1990a) determined several kinematic parameters for bumblebees in forward flight (body angle, stroke plane angle, geometrical angle of attack, etc.) varied consistently with airspeed. Dudley and Ellington (1990b) showed that quasi-steady aerodynamic mechanisms were insufficient to explain the fast forward flight of bumblebees. Ortega-Jimenez et al (2013) experimentally determined the kinematic effects of moths flying into vortices.

In computational study, 3D computational fluid dynamics (CFD) has allowed researchers to study the unsteady flow and force production associated with animal wings. For example, Sun and Tang (2002) modeled a fruit fly wing in a flapping motion and found when the wing rotation occurs at the end of a stroke, the mean lift coefficient can be two times greater than the quasi-steady value. Liu and Kawachi (1998) numerically modeled a hawkmoths wing during hovering flight and compared the numerical results with smoke-visualized flows around a manmade flapper. Some of these computational studies have incorporated realistic wing motion obtained through measurement of high-speed videography and have involved multi-disciplinary collaborations between fluid dynamists who seek to understand the phenomenon involved in flapping wings and biologists who seek to understand how it relates to live animal flight. For example, Song et al (2014) developed a CFD model for hovering flight of the hummingbird and studied detailed force production of downstroke and upstroke; later, the authors (Song et al, 2016) used a similar approach to study forward flight of the hummingbird and compared its aerodynamics with that of insects and large birds.

The second direction of study is investigation of basic fluid dynamics involved in flapping wings. Wang (2005) provides a thorough literature review in insect flight and discusses the unsteady mechanisms for uniform and accelerated motions. For this purpose, very simple wing shape and kinematics could be adopted in the study, for example, an airfoil performing sinusoidal pitching and/or heaving motions. Sometimes even 2D models are very useful, and the effects of linear acceleration and pitching on vortex formation, flow separation, and unsteady forces are usually main foci of this type of studies. For example, Wang et al (2004) compared 2D computations with 3D experiments and found in all cases, the computed drag compared well with the experimental

drag and the computed lift agreed with the experimental lift when the sinusoidal changes in angle of attack were symmetrical. Of course, only simple wing geometry and kinematics were used for comparison.

In addition to rigid wing models, there have been studies to incorporate elasticity of flapping wings that investigate the effect of fluid-structure interaction and aeroelasticity on aerodynamic performance of the wings. Yin & Luo (2010) found that both inertia-induced deformation and flow-induced deformation can both enhance lift of an elastic wing. Similarly, Dai et al (2012) demonstrated that deformation not only enhances lift but also improves the lift efficiency even with an unfavorable camber. Eldredge et al (2010) discovered that a flexible wing consistently demonstrated better performance than a rigid wing due to how the leading-edge vortex shed into the wake during the return stroke, this led to less interaction with the previously shed trailing-edge vortices. From these and several other studies, it is clear that proper structural elasticity would significantly improve aerodynamic performance of flapping wings.

Other than steady flight, bio-inspired transient aerodynamic maneuver studies are a growing subject of interest as UAVs are becoming as popular as ever. In this area, again both animal studies and simplifying model studies were carried out. For example, Carruthers et al (2007) observed that a steppe eagle performing a perching maneuver gained altitude quickly during the landing phase, implying that large lift was required at high angles of attack. Specifically, the perching aerodynamic maneuver provides the ability for a UAV to land precisely on a narrow platform without the requirement to decelerate on the ground like typical fixed-wing UAVs. Even with Cory and Tedrake (2008) recent advances that demonstrated the ability for current MAVs to land on a perch, these MAVs still fall short in achieving the stability and control, speed, and overall elegance of the natural flyers that we seek to emulate. Polet et al (2015) investigated a simple pitch-up maneuver that linearly deaccelerates and further validated that a perching bird can maintain high lift and drag while slowing to a controlled stop despite the large angles of attack and decreasing flow velocity. Using particle image velocimetry (PIV) and simulations, Polet et al (2015) studied the differences in forces and vorticity fields as the pitch rate increased and found that the lift and drag forces increase super-linearly with the pitch rate (or shape change number).

Reduced-order aerodynamic models that can faithfully capture the unsteady flow are a key area of research for successful engineering applications of flapping wings. Many parallel efforts are ongoing with various levels of success. For example, Wang and Eldredge (2012) created a low-order model to predict the dynamics of the leading edge vortex (LEV) during both pitching and perching maneuvers. Wang and Eldredge (2012) low-order (e.g., less than ten degrees of freedom) impulse matching approach enabled more accurate force predictions on 2-D pitching and perching maneuvers than the Brown-Michael model when compared with both experiments and high-fidelity simulations.

I.3   The specific objectives of this study

In general, acceleration and deceleration of the wing, as well as rotation around the wing axis, are critical features of flapping wings, but the fundamental fluid dynamics is not yet well understood. Basically, there is a lack of simple models that can accurately describe force production in relation

with the wing velocity, acceleration, rotational velocity, and rotational acceleration. This thesis aims to better understand how the wing-pitching affects the force production, boundary layer detachment, and vortex formation in the flow. For this purpose, extremely simplified cases are considered, i.e., the pitching-only and perching wings, and this study numerically simulates the flow to obtain the unsteady velocity field, pressure distribution, and total lift and drag. Their dependence on the wing motion will be studied.

To be more specific, in this thesis I aim to investigate the viscous, unsteady flow over a NACA 0012 airfoil that pitches to a high angle of attack (α) by using a 2D laminar flow and time-dependent study. For the perching maneuver, the airfoil is also assumed to go through a deceleration process while pitching. Since flow separation and vortex generation are going to be dominant features of the flow, the effect of viscosity has to be included in the computational model to accurately predict these unsteady flow behaviors. For this investigation, a rigid wing is assumed in order to simplify the problem. To validate the simulation, I will first compare the results in this study with the results of Polet et al (2015) and Wang and Eldredge (2012). After model validation, I will then move on to study details of flow in two separate scenarios: (1) a controlled pitch-up maneuver and (2) a perching maneuver where the wing experiences simultaneous deceleration and pitching motion.

Chapter II   Model description and validation

II.1   Description of the wing model and simulation setup

To investigate the fundamental unsteady fluid dynamics and force production of flapping wings, highly simplified situations where wings only perform combined linear translational and pitching motion were considered. In addition, three-dimensional (3D) effects were ignored and this study concentrated only on two-dimensional (2D) models. (Carruthers et al., 2007)

Consider a NACA0012 airfoil that is immersed in a uniform fluid traveling at a time-varying velocity, U(t). The airfoil is initially at an angle of attack α=0° and is made to rapidly pitch up to α=90° at an angular velocity $\omega(t)$. Two distinct classes of translational motion are considered, first pitching where U(t)= U_0, a constant velocity, and then perching which Granlund et al (2010) defines as the airfoil linearly decelerates from the initial velocity U_0 to rest during the pitch-up maneuver. A perching maneuver performed by a Steppe Eagle Aquila nipalenis is shown in Figure 1.

Figure 1: Visualization of perching maneuver by Carruthers et al (Carruthers et al., 2007)

Commercial package COMSOL Multiphysics 4.4 was chosen to model this problem using its Rotating Machinery module. COMSOL Multiphysics is a finite-element modeling, simulation, and visualization software package that has a friendly user interface and a much more forgiving learning curve than some in-house packages, e.g., a boundary data immersion method (BDIM) that Zhao et al (2011) use or the viscous vortex particle method (VVPM) used by Peskin and Dora (2002) while still providing impressive accuracy results. The NACA0012 airfoil profile was imported into COMSOL Multiphysics using 140 data points to ensure that enough resolution could be achieved around the airfoil. The computational domain is a square box shown in Figure 2. The following boundary conditions were applied: the left side of the square is designated as the inlet, the right side is the outlet, and both the top and bottom are open flow boundaries. The inside of the circle enclosing the airfoil is set as a rotating domain, for which the rotational velocity and rotational axis are specified. The rotating wall node in COMSOL is a boundary condition that is applied to the airfoil, which essentially represents the no-slip condition for the fluid at the airfoil surface. Fluid continuity is specified along the perimeter of the circle and is suitable for pairs where the boundaries match; it prescribes that the flow field is continuous across the pair. The freestream flow speed at the inlet is U(t); thus the airfoil does not have to translate in the domain. To account for the non-zero inertial effect that results from the deceleration of the airfoil in the actual situation, a uniform volumetric force is included for the perching case to decelerate the flow correspondingly. The uniform volumetric force is given by Eq. (1) below,

$$\rho \frac{\partial U(t)}{\partial t} \tag{1}$$
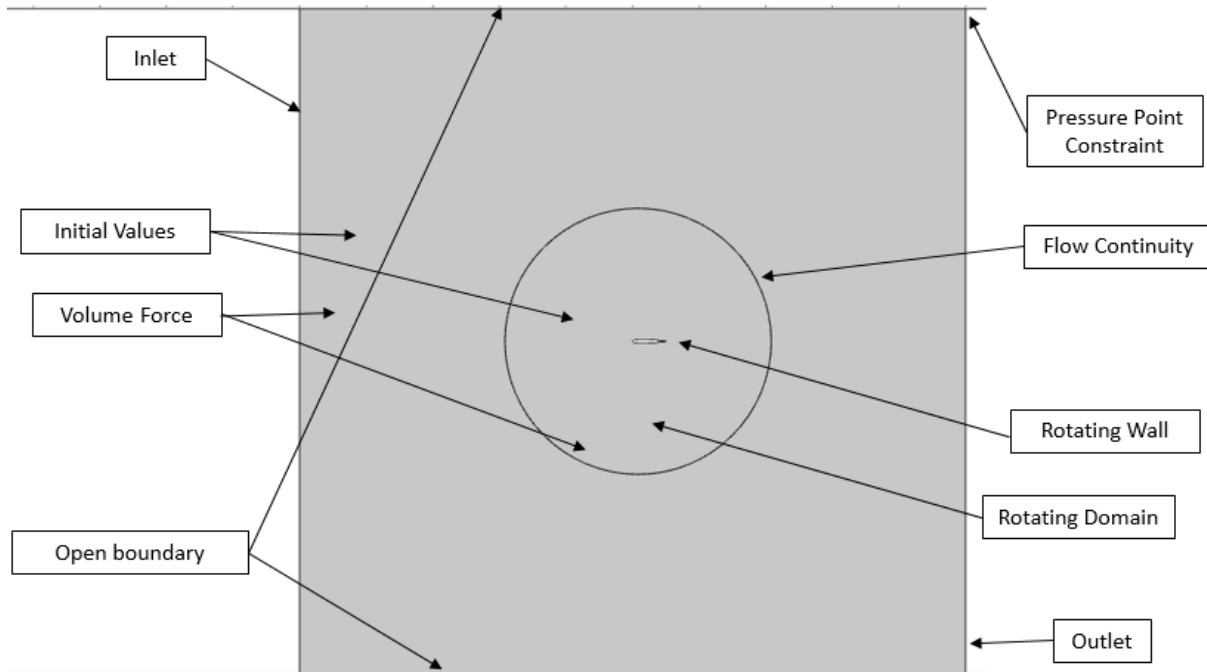
Figure 2: Illustration of the complete computational domain with boundary conditions

The mesh discretization is shown in Figure 3. It can be seen that the flow field immediately surrounding the airfoil has a much finer mesh in the area of interest (domain 1 is inside the cycle) than domain 2 (outside of the circle); this was done to resolve the vortices around the airfoil while minimizing the overall computational cost. Note that the two domains are meshed separately but share the same mesh nodes along the domain interface (the circle); this ensures that mesh continuity across the two domains. The mesh was created using a two part mesh in COMSOL. The first part uses COMSOL's pre-defined 'fine' setting for the outside domain (outside of the circle) while the inner domain (inside the circle) uses a user-controlled custom mesh. Adjusting the size parameters from the 'extremely fine' default settings within the circle domain; the maximum element size limits how large each individual mesh element can be, which is set to be 0.134 times the chord length (c); while the maximum element growth rate limits the size ratio between two adjacent mesh elements and is set to be 1.02c; therefore, lowering both of these parameters created a much finer mesh for the inner domain. The predefined 'fine' mesh setting was utilized on the outer domain, the maximum element size was 1.34c and the maximum element growth rate was 1.13c. The inner domain, outer domain and total combined mesh consisted of 154,640, 2,154, and 156,784 elements respectively and can be seen in the zoomed in view shown in Figure 3.
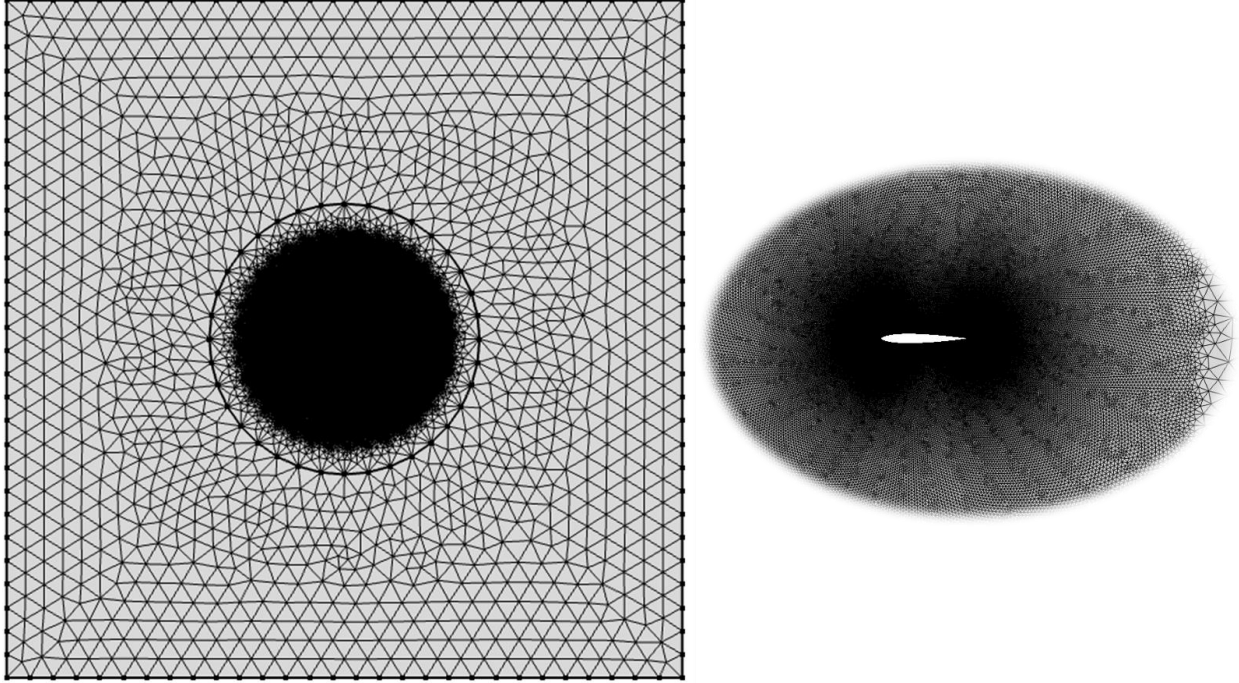
Figure 3: Mesh used in the simulation, where the inner region and outer region were meshed separately

II.2   Validation study: case 1

Two validation cases were carried out to verify the current model setup and assess the accuracy of COMOSL simulation. In the first validation study, the perching maneuver kinematics as specified in Polet et al (2015) were used, where the time-dependent inlet velocity and angle of attack are given as functions of time as:

$$U = U_0(1 - t^*) \tag{2}$$

$$\alpha(t) = \frac{\pi}{2}\left[t^* - \frac{sin(2\pi t^*)}{2\pi}\right] \tag{3}$$

Here t^* is the non-dimensional time ($0 \leq t^* \leq 1$) and is defined as $t^* = t/T$, where t is the actual time, and T the total time period for the airfoil to complete the perching maneuver. Eq. (3) is incorporated into the COMSOL model by specifying the angular velocity located in the rotating

domain section; this requires taking the time derivative of Eq. (3), which produces the following angular velocity equation,

$$\omega(t) = \frac{\pi}{2}\left[\frac{1}{T} - \frac{cos(2\pi t^*)}{T}\right] \tag{4}$$

In order to compare the results with those in Polet et al (2015), the flow conditions were non-dimensionalized. The current study was limited to low Reynolds number aerodynamics, where both the boundary layer and the bulk fluid are laminar. Consider the viscous, incompressible unsteady flow over a NACA 0012 airfoil that has a chord length c=1.0 m, under the following conditions: initial velocity U_0 =1 m/s, fluid density ρ =1.0 kg/m3, and dynamic viscosity μ =0.0005 Pa•s. The Reynolds number can be thus calculated according to the following equation:

$$Re = \frac{\rho U_0 c}{\mu} \tag{5}$$

This Reynolds number of 2,000 matches the Reynolds number in Polet et al (2015). In that reference, the shape change number (SC) is used to parametrize the ratio between the translational speed and the rotational speed, or rate of the shape change of the system (as viewed by the flow). Here the shape change number and pitch rate, K, are used interchangeably which is defined as:

$$SC = K = \frac{c}{T\, U_0} \tag{6}$$

The center of pitch rotation was located c/6 from the leading edge.

II.3   Results from validation case 1

Three simulations were conducted keeping other parameters constant except the value of pitching time, which is T= 2, 4 and 8 seconds. These aforementioned values of T lead to three distinct pitch rates, from fastest to slowest, K=$\frac{1}{2}$,$\frac{1}{4}$ and $\frac{1}{8}$.

The forces the airfoil experiences for the three different pitch rates are shown in Figure 4 along with the reference results. The lift and drag coefficients, Cl and Cd, are defined using the chord length c, fluid density ρ, and velocity U_0. Looking at the lift and drag coefficients as functions of the non-dimensionalized time, it can be seen that in all three cases lift reaches the maximum value at approximately t*=0.44 and drag reaches the maximum around t*=0.51. Note that there is a general trend for both lift and drag: as the pitch rate increases, so does the magnitudes of the forces. Most importantly, the results shown here are in very good agreement with the results in Polet et al (2015).

To visualize the flow field in this study, we plot the vorticity and pressure contours, both of which are normalized properly. Unless specified otherwise, the vorticity is normalized by U_0/c, and the pressure is normalized by ρU_0^2.
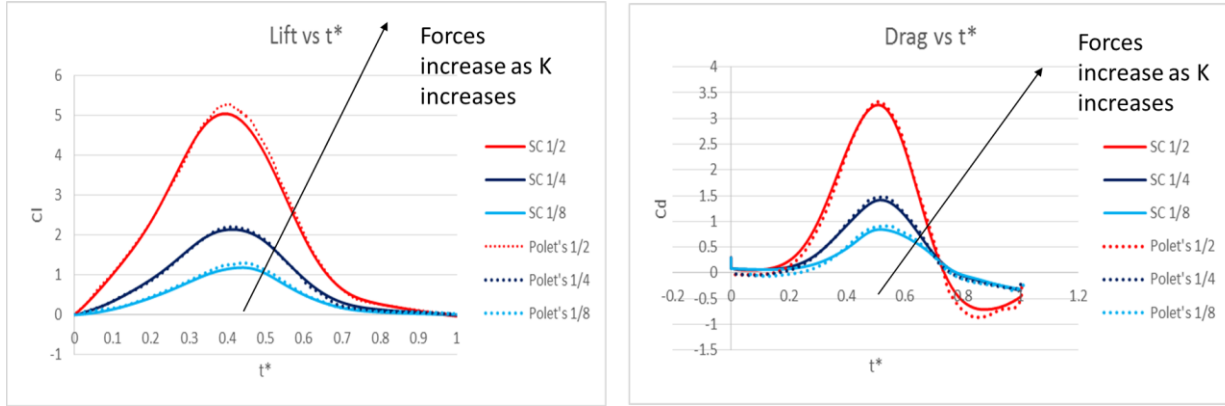
Figure 4: Lift and drag coefficients for three pitch rates. Solid lines represent the current study, and dashed lines are the results from Polet et al (Polet et al., 2015)

The vorticity fields are shown Figure 5 and Figure 6 that result from the perching maneuver for pitch rates ¼ and ½, which represent moderate and fast pitching, respectively. The top panel of the figure is the results from Polet et al (2015), where the first row of plots is for experimental results and the second row is for the numerical simulations. It can be seen from these two figures that the current simulation results are in good agreement with those in the reference, including both numerical and experimental data. In particular, the vortex structures in the current simulations, such as the leading edge and trailing edge vortices, have similar patterns as those simulated by Polet et al (2015), which are in turn consistent with experiment observation. The experiment was carried in a water tunnel and particle imaging velocimetry (PIV) was used to measure the flow field and derive vorticity. In addition to vortex patterns, the formation time and convection of the vortices from the airfoil, as measured by the distance between the vortices and the airfoil, are consistent between our results and those in the reference. It is also worth noting that for both pitch rates, the horizontal distance between the leading edge and trailing edge vortices is decreasing as the airfoil is increasing its angle of attack.

Unsteady dynamics of rapid perching manoeuvres
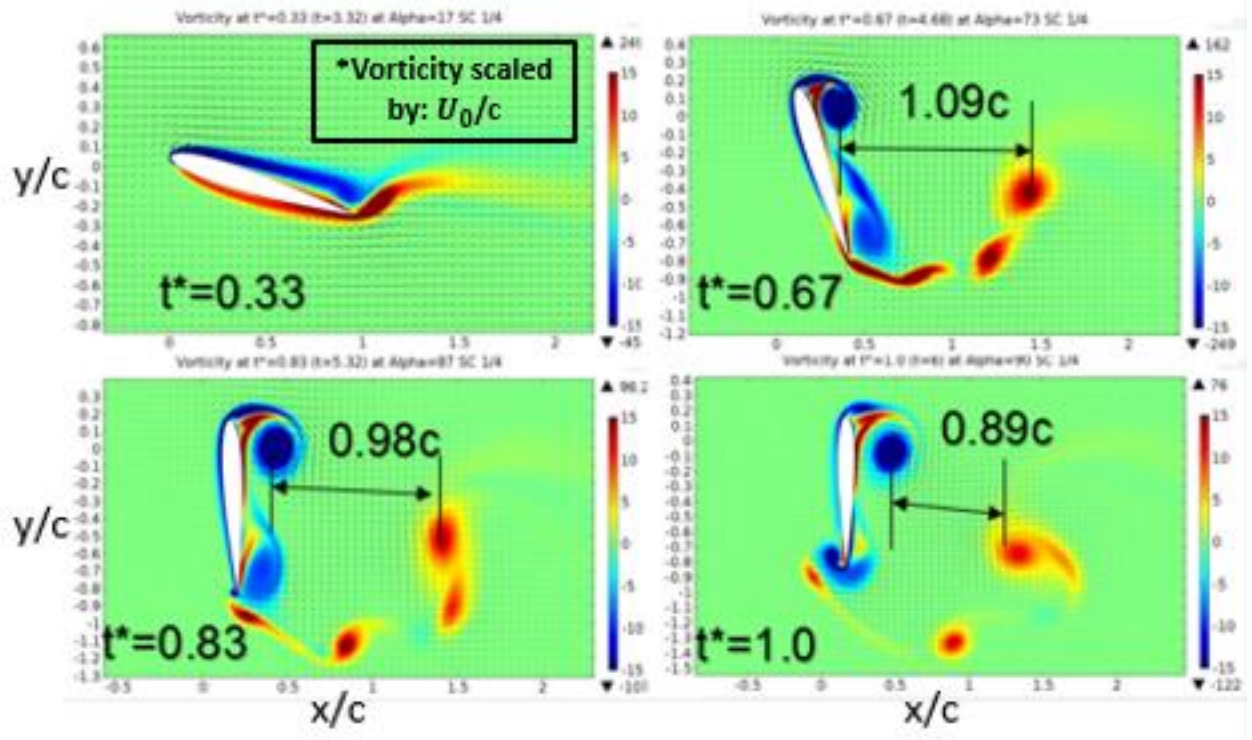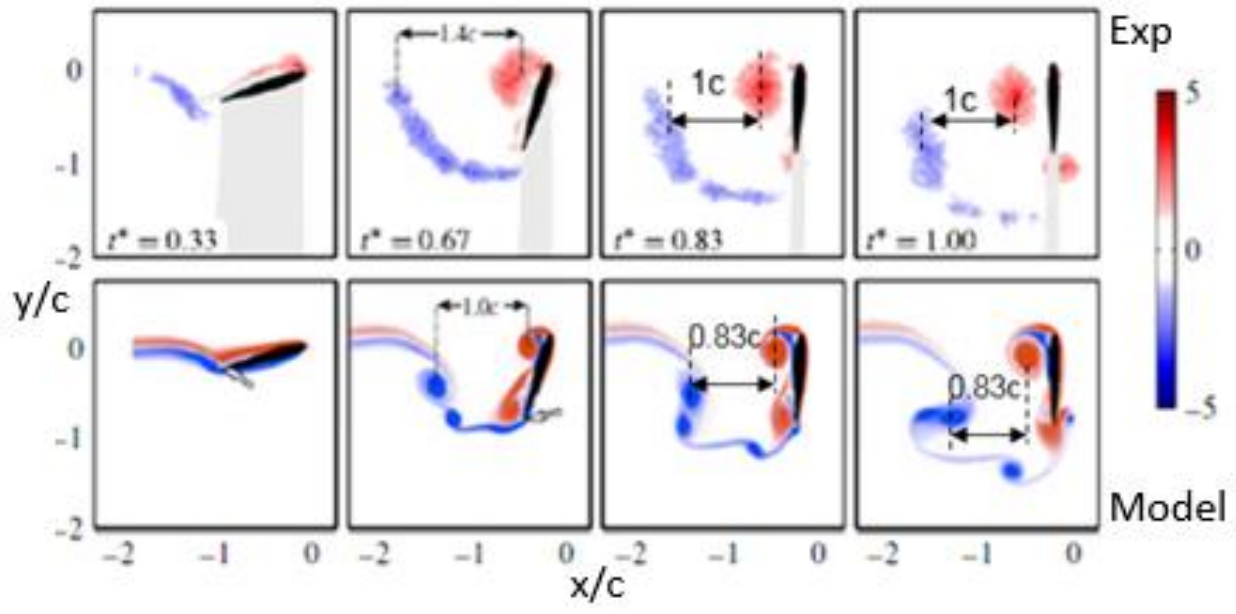
Figure 5: Vorticity field of perching motion with K =1/4 at α = 17°, 73°, 87°, 90°. Upper panel: results from Polet et al (2015); lower panel: present study.
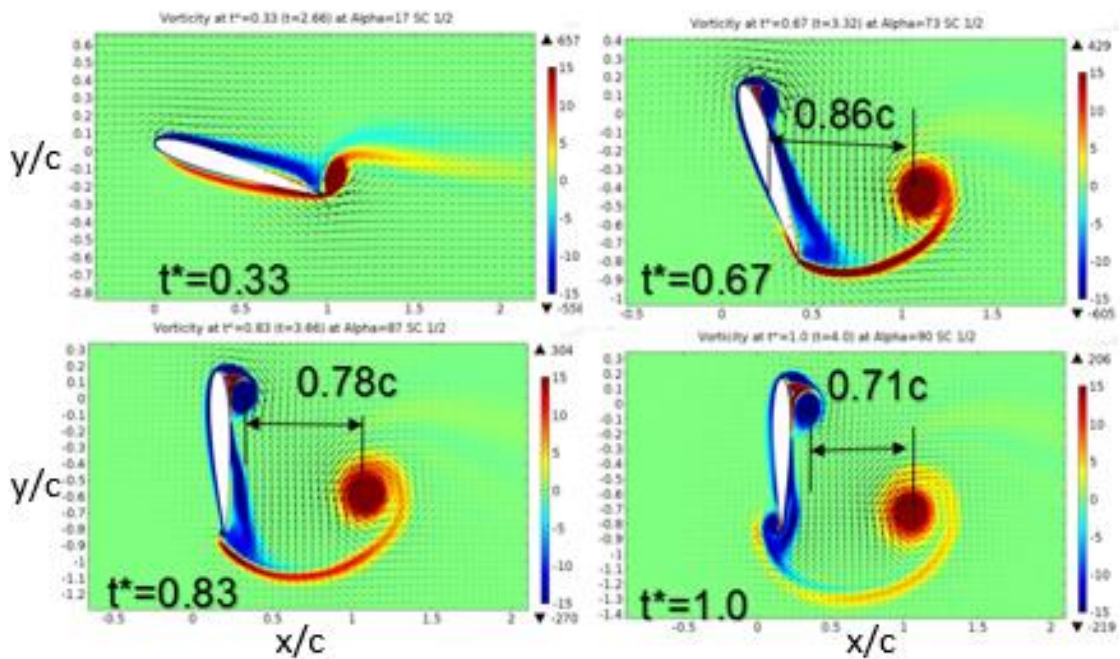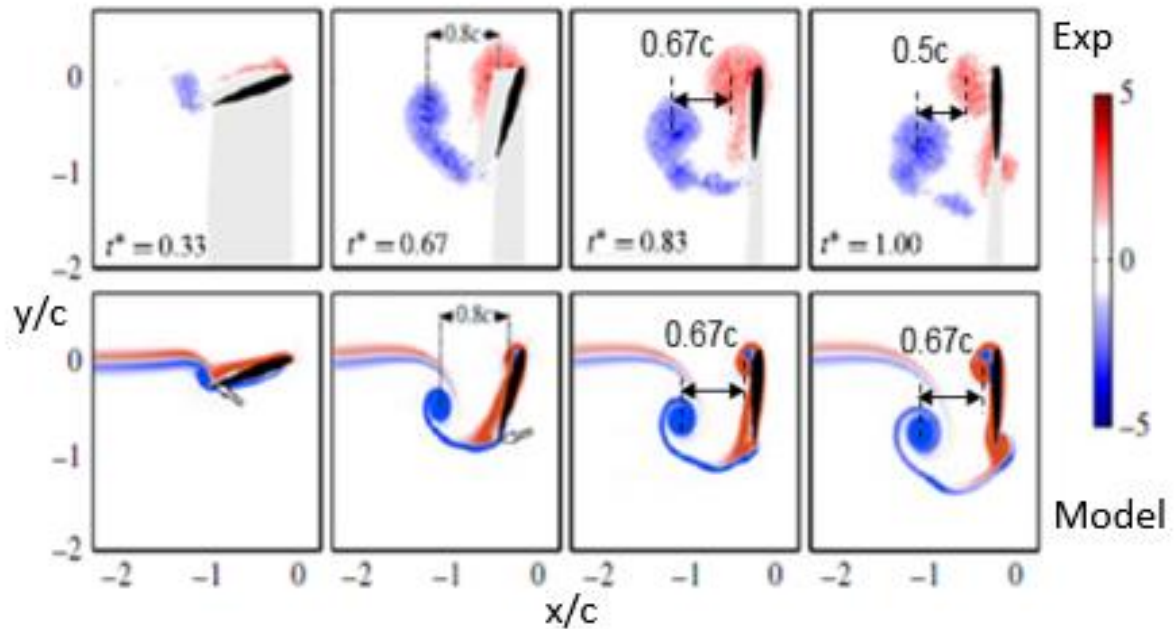
Figure 6: Vorticity field of perching motion with K =1/2 at α = 17°, 73°, 87°, 90°. Upper panel: results from Polet et al (2015); lower panel: present study.

II.4   Validation study: case 2

A second validation case was considered, where the airfoil performs either pitching or perching motion, and the case was numerically studied by Wang and Eldredge (2012) using a highly accurate viscous vortex particle method. In this case study, the time-dependent angle of attack is given by:

$$\alpha(t) = \frac{\alpha_o \log\left[\frac{\cosh(\frac{a_s U_0(t-t_1)}{c})}{\cosh(\frac{a_s U_0(t-t_2)}{c})}\right] - a_s U_0(t_1-t_2)}{2a_s U_0(t_2-t_1)/c} \tag{5}$$

Where the smoothing parameter a_s controls the speed of the transitions between kinematic intervals, t_1 and t_2 are the start and stop instances for the pitch-up maneuver, and α_o is the maximum angle and is set to be $\pi/2$.

The Reynolds number, defined in the same way as before, is set at Re=1,000 for comparison purposes. Wang and Eldredge (2012) defines the nominal pitch rate, $\dot{\alpha}_o$, by setting the value of a dimensionless pitch rate, k:

$$k = \frac{\dot{\alpha}_o C}{2U_0} \tag{5}$$

Two different types of translational motion were considered; the first is pitching where U(t)= U_0 (i.e., constant speed) and the second case is perching which is defined by Granlund et al (2010), where the wing starts at an initial speed U_0 and decelerates linearly until rest during the pitch-up maneuver. For the both cases, the pitch axis is located at the leading edge.

II.5   Results from validation case 2

The lift and drag forces produced during the pitching maneuver are first compared and are shown in Figure 7. Two pitch rates are considered here, k=0.2 (slower pitching) and k=0.7 (faster pitching). As shown in the figure, the present results are overall consistent with those in the Wang and Eldredge (2012). For the slower pitch rate case, k=0.2, the matching is better as compared with that for the faster pitch rate, k=0.7. However, neither case agrees as strongly as in validation case study 1. This is likely because in case study 1, both our simulation and the reference study used the same NACA airfoil, while in the current case study, Wang and Eldredge (2012) used a flat plat with rounded leading and trailing edges and the plate thickness is 0.023c. Such difference in the geometry of the airfoil likely have caused the discrepancy seen in the validation.
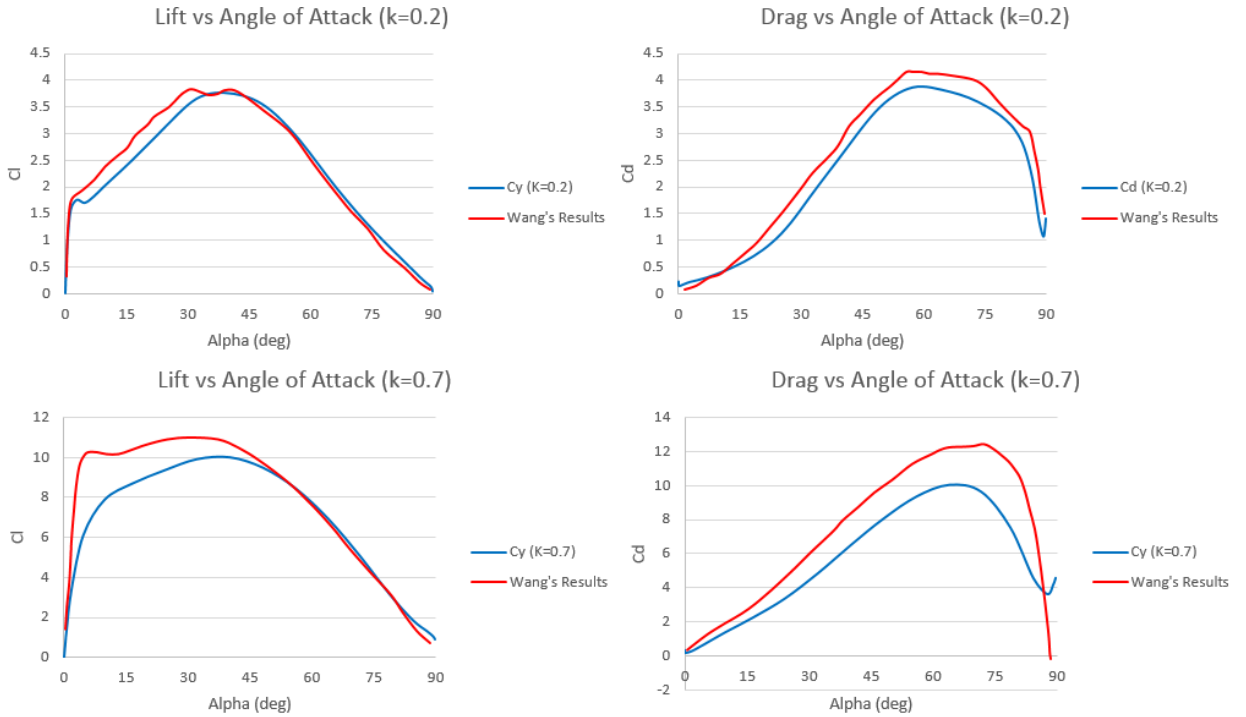
Figure 7: Comparison of lift and drag coefficients of a pitching wing at k=0.2 and k=0.7

The vorticity fields at three distinct angles of attack, or time moments, during the pitching maneuver at k=0.2 are shown in Figure 8 By comparing the results obtained during this investigation (left column) with the results described in Want and Eldredge (2012), both experimentally and numerically (middle and right column), it can be seen that the flow fields of all three studies are very similar. A starting vortex at the trailing edge, or trailing-edge vortex (TEV) is generated first, and the leading-edge vortex (LEV) forms at a later time during the pitch-up maneuver. The LEV remains close to low pressure side of the airfoil, while initial TEV is significantly further downstream. The distance between the LEV and TEV is measured for angle of attack at 53 and 90 deg., and the result appears to be in good agreement with that in the reference.
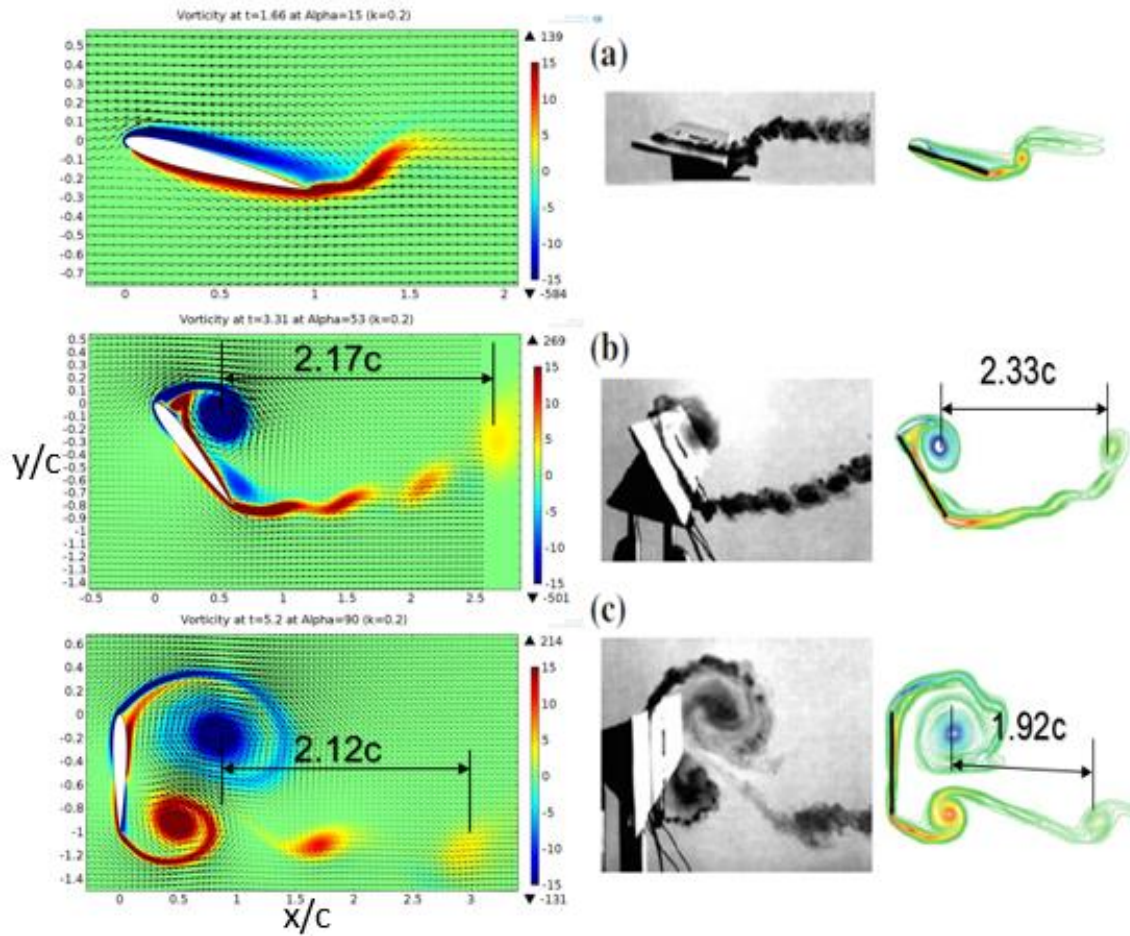
Figure 8: Flow field of pitching motion for k=0.2 at α = 15°, 53°, 90°. The results in the middle and right columns are from Wang and Eldredge (2012)

The flow field for the pitch rate of k=0.7 at angles of attack 33 and 90 deg are shown in Figure 9. It can be easily seen that the flow fields are very similar for this case as well. Looking at α = 90 deg, the flow separation on the suction side near the trailing edge is present in both studies, and both studies have a similar distance between the leading-edge and trailing-edge vortices. The main discrepancy between the two studies appears to be at α = 33 deg, where the LEV from the present simulation is not completely formed or as distinct as it is in Wang and Eldredge (2012). This difference is again likely due to the rounded edges and smaller thickness of the plate used in Wang et al.
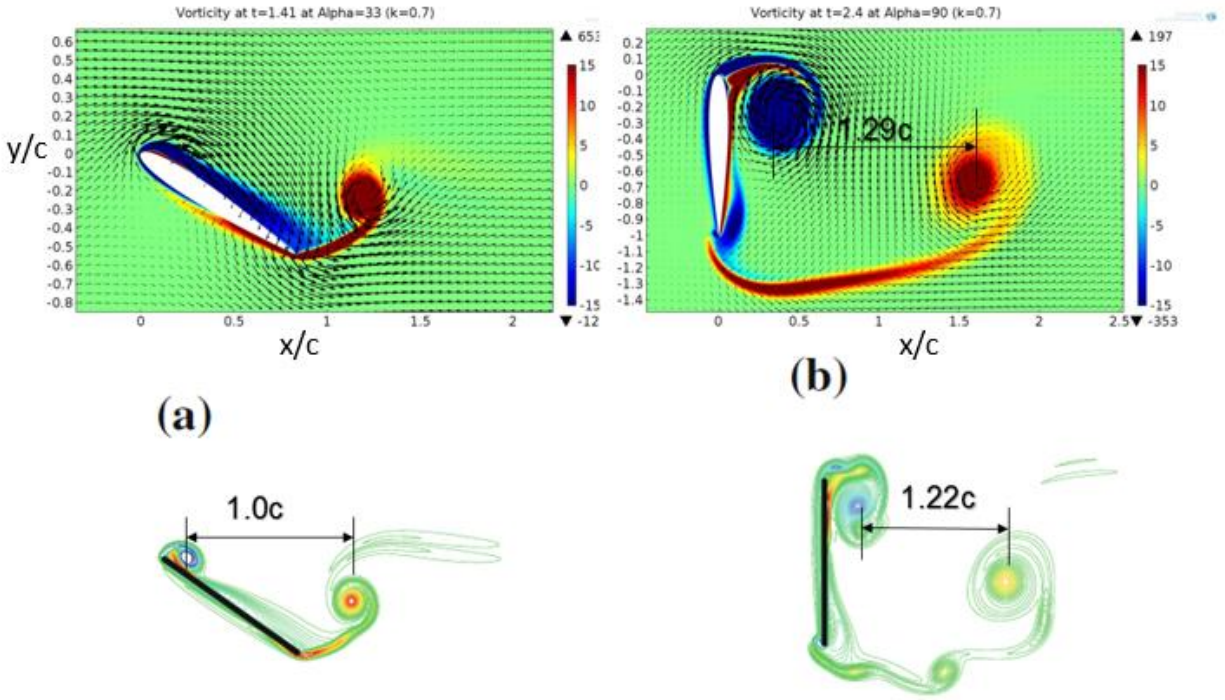
Figure 9: Flow field of pitching motion for k=0.7 at $\alpha = 33°$ and 90°. Top: present study; bottom: results from Wang and Eldredge (2012)
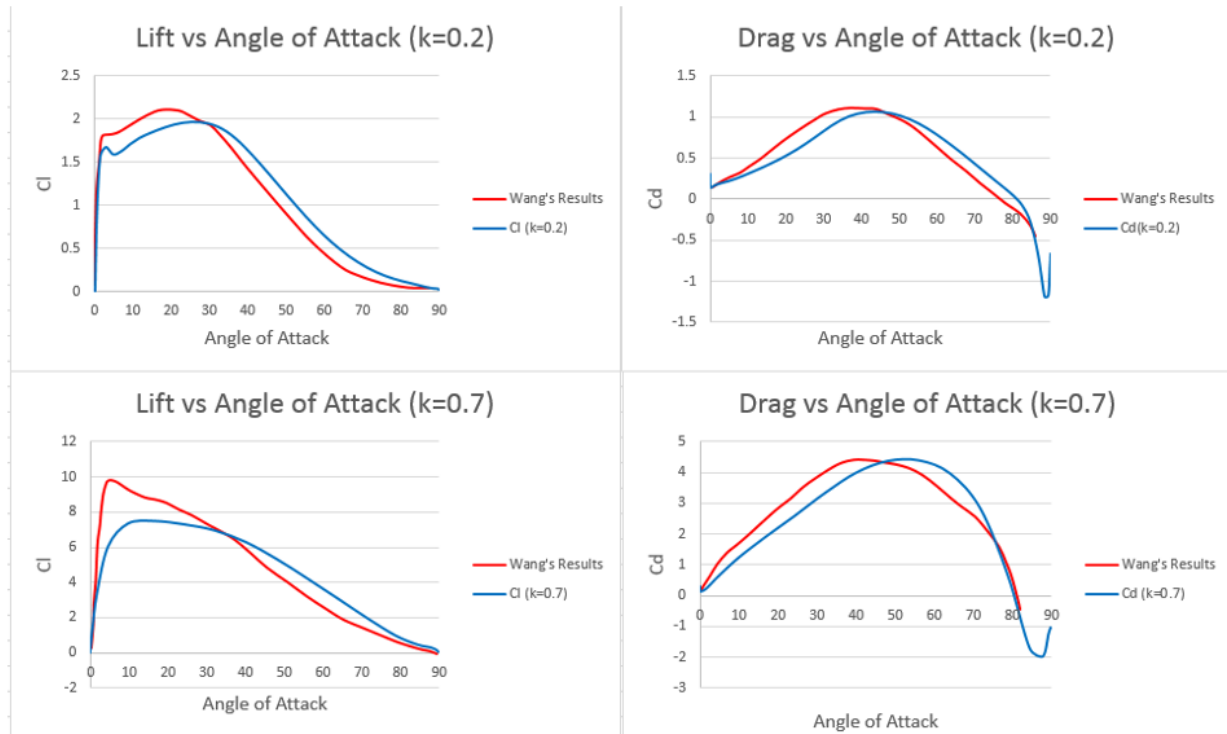
Figure 10: Force production comparison for k=0.2 and 0.7 for perching cases

Next the perching maneuver study is examined. The lift and drag coefficients are shown in Figure 10 for k=0.2 and 0.7. As in the pitching maneuver study, the agreement between our results and those from Wang and Eldredge (2012) is better for the slower pitch rate (k=0.2) than for the faster pitch rate (k=0.7). Nevertheless, the agreement is generally acceptable. Due to differences in the airfoil geometry, result matching is not as strong as that in the validation case study 1.

The flow field for these two cases is shown in Figure 11 and Figure 12. In Figure 11 where k=0.2, the LEV remains close to the suction side, while the TEV is convected further downstream. The LEV travels slightly further downstream between 53 and 90 deg; this corresponds to the drop in lift that is produced when pitched at such extreme angles of attack. The LEV and TEV appear to be in good agreement for the current simulation and Wang and Eldredge (2012), particularly so when $\alpha° = 53$ deg.

Again, the agreement at k=0.7 between our study and Wang and Eldredge (2012) can be seen in Figure 12. It can be seen that the LEV is significantly closer to the suction side of the airfoil for k=0.7 as compared to when k=0.2 in the previous figure. This LEV proximity even at high angles of attack is what provides the necessary lift for the perching maneuver. The distance between the LEV and TEV is significantly smaller for this faster pitch rate.
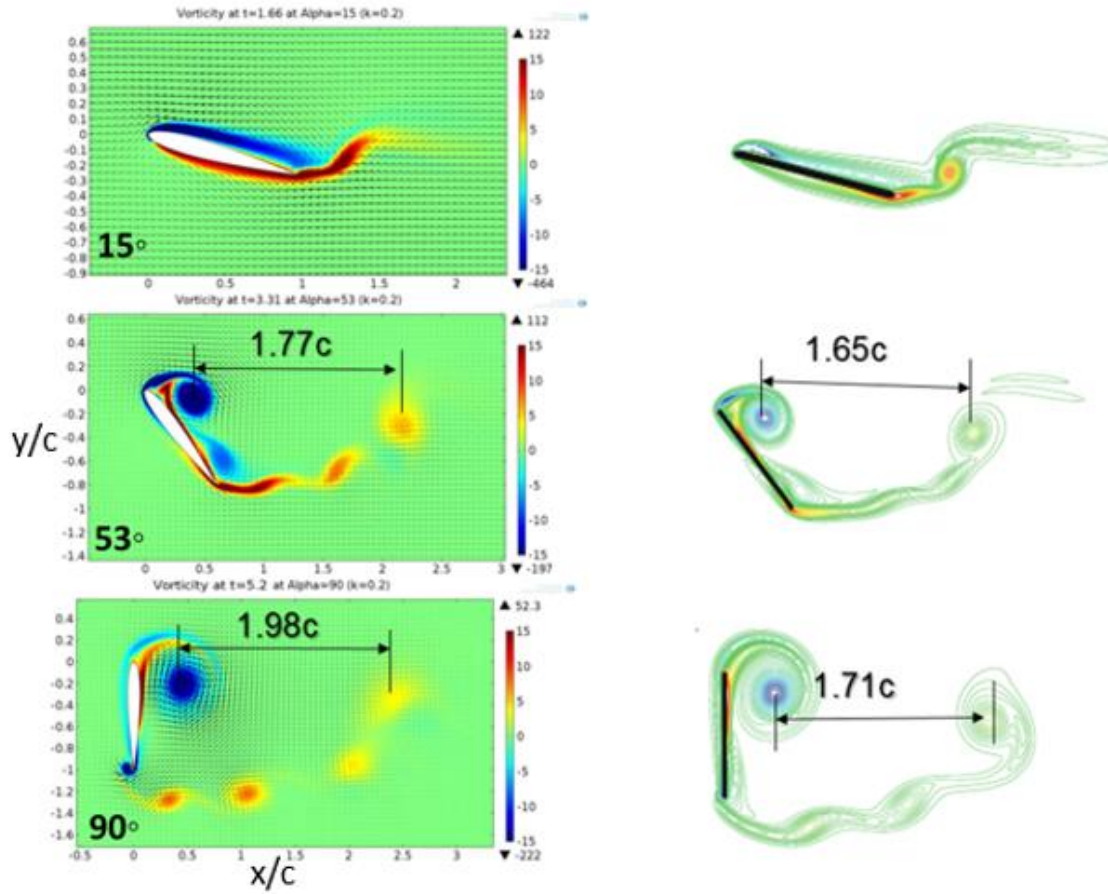
Figure 11: Flow field of perching motion for k=0.2 at α = 15°, 53° and 90°. Left: present study; right: results from Wang and Eldredge (2012)
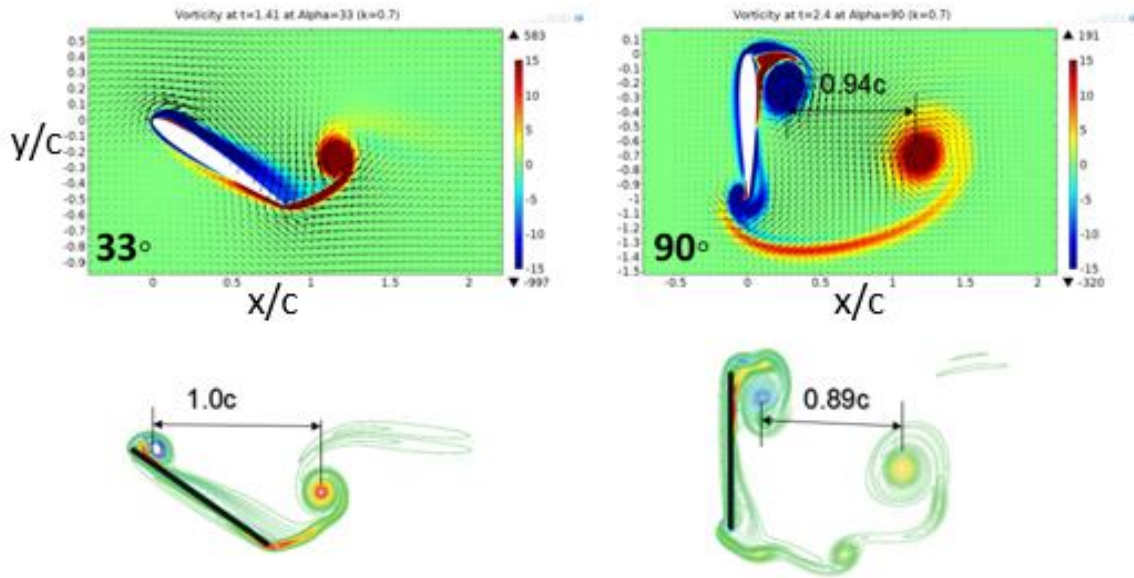
Figure 12: Flow field of perching motion for k=0.7 at $\alpha = 33°$ and 90°. Top: present study; bottom: results from Wang and Eldredge (2012)

To summarize this chapter, I have performed two validation studies for the present flapping wing model against previous numerical and experimental studies and have carefully examined the force production and flow field of both pitching maneuver and perching maneuver. The agreement with previous data is overall satisfactory. These successful validations show that my COMSOL model setup (including the use of the rotating framework and a non-inertial coordinate system), assumptions, and mesh design are all correct or appropriate. Next, I will move forward to study details of unsteady fluid dynamics involved in pitching and perching maneuvers.

Chapter III Unsteady aerodynamics of a pitching airfoil

In this chapter, I will describe the results for an airfoil immersed in a uniform flow while performing the prescribed pitching motion. I will discuss the force production, pressure distribution, vorticity field, and their dependence on the pitch rate. The model assumptions and simulation setup have been described in Chapter II. For the current pitching airfoil, the freestream velocity is set to be constant. Simulation for a stationary airfoil at zero deg angle of attack was run first to achieve the steady state of the flow; then the airfoil performs the pitching motion as prescribed by the sinusoidal function in Eq. (3) at time $t=0$. The pitch rate is set to be 1/2 (fastest), 1/4, 1/8, and 1/64 (slowest).

III.1   Force production

The lift and drag generated by the NACA 0012 airfoil are shown below in Figure 13. It can be seen that as the pitch rate (K) increases, so do the peak lift and drag that are produced. Except for the case of slowest pitching at K=1/64, in the other cases, lift and drag generally first increase and then decrease. Note that neither the lift or drag peak at consistent times or angles across the different pitch rates, even though the angular velocity always has a maximum at 45 deg. The angular velocity as a function of angle of attack is shown in Figure 14. Looking at fastest pitching at K=1/2, the lift peaks at approximately $\alpha = 38$ deg while the drag doesn't peak until $\alpha = 60$ deg. For K=1/4 and 1/8, the lift peak is slightly delayed to a great angle of attack; however, the drag peak is not consistently varying. Specifically, the peak drag for K=1/4 is Cd = 5.11 at $\alpha = 66$ deg, and for K=1/8 is Cd = 3.61 at $\alpha = 56$ deg. The detailed statistics are tabulated in Table 1 for easy comparison. For K=1/64, lift and drag become highly oscillatory when α is greater than 20 deg., which indicates that vortex shedding is happening, as in the case of a stationary airfoil at stall state. Comparing the different pitch rates, the Cl/Cd remains favorable until $\alpha = 52, 50, 47$ and 41 deg for pitch rates k= ½, ¼, 1/8 and 1/64, respectively. That is, the pitch motion clearly has delayed stall and provided enhancement to the airfoil performance.

21
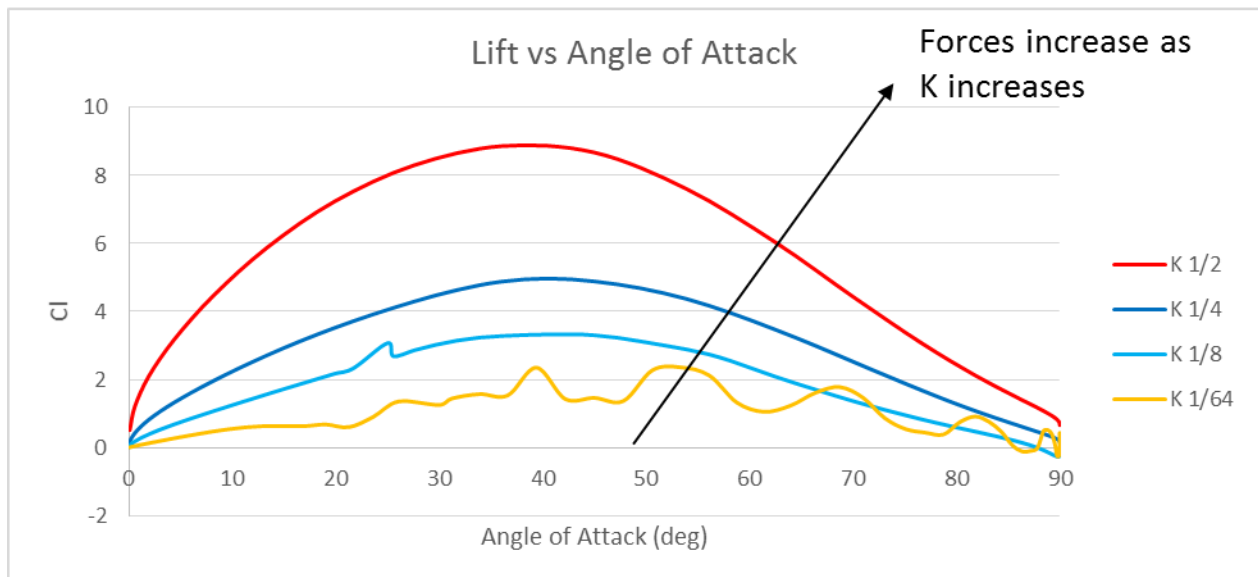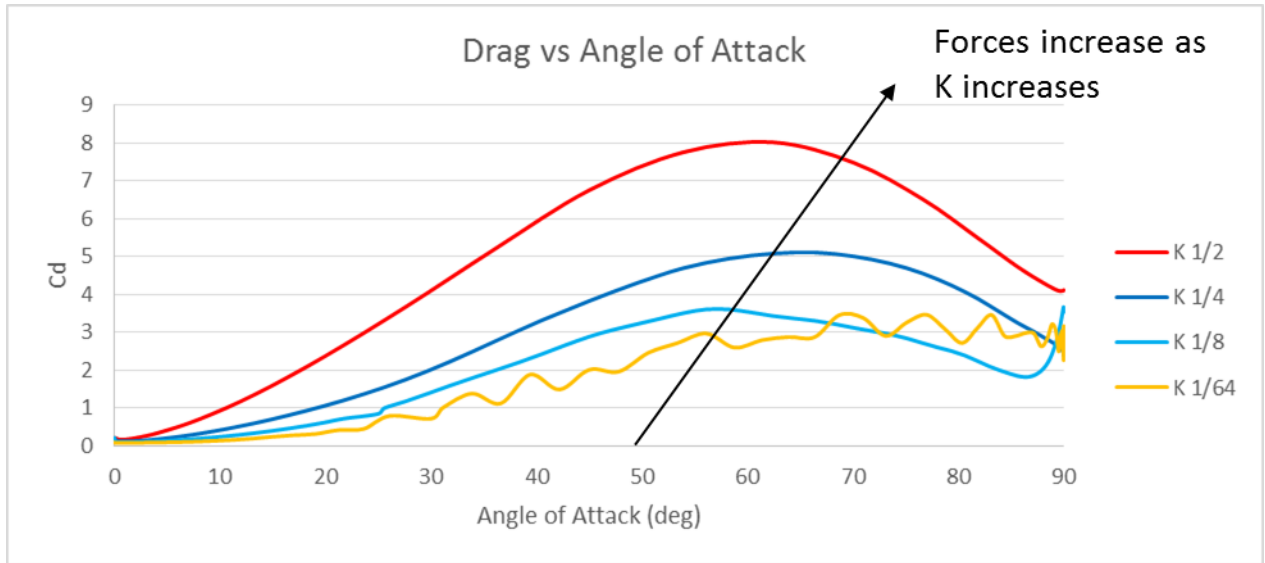
Figure 13: Lift (top) and drag (bottom) coeffcients as a function of angle of attack,α, for K = 1/2, 1/4, 1/8 and 1/64
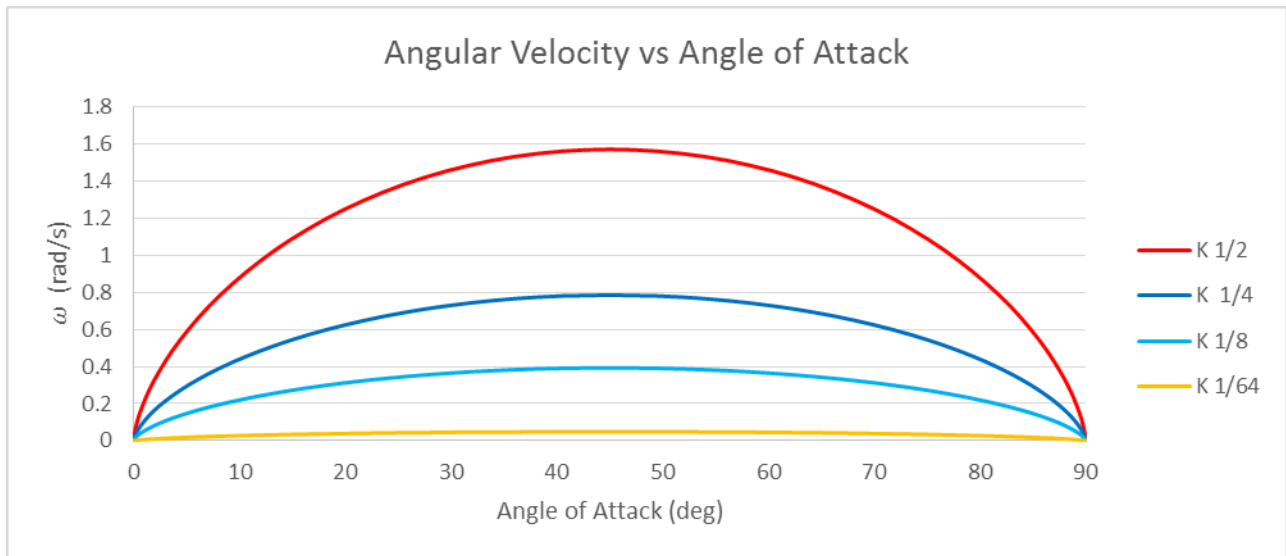
Figure 14: Specified angular velocity as a function of angle of attack for K = 1/2, 1/4, 1/8 and 1/64.

K	Max Cl at α		Max Cd at α		Max Cl/Cd at α		Avg Cl	Avg Cd	Avg Cl/Cd
1/2	8.91	38.28	8.01	60.36	10.01	1.91	3.92	3.81	1.03
1/4	4.97	40.51	5.11	66.38	6.94	4.38	1.99	2.36	0.84
1/8	3.33	42.75	3.61	56.11	5.44	6.10	1.15	1.77	0.65
1/64	2.36	53.38	3.46	68.73	3.91	8.18	0.67	1.68	0.40

Table 1: Detailed lift and drag statistics for the pitching airfoil (note that the spike in the drag history for the case of K=1/8 was ignored)

The lift over drag ratio that was generated by the NACA 0012 airfoil is shown in Figure 15 . It can be seen that as the pitch rate K increases, so do the peak lift over drag ratios that are produced. As the pitch rate increases, the lift over drag peaks at a smaller α. Looking at fastest pitching at K=1/2, the lift over drag peaks at a Cl/Cd=10.01 at approximately $\alpha = 2$ deg. For K=1/4, 1/8, and 1/64, the lift over drag peaks are slightly delayed to larger angles of attack; the lift over drag ratios peak approximately 2 deg later between the pitch rates. Specifically, the peak lift over drag for K=1/4 is Cl/Cd = 6.94 at $\alpha = 4$ deg, for K=1/8 is Cl/Cd = 5.44 at $\alpha = 6$ deg, and for K=1/64 is Cl/Cd = 3.91 at $\alpha = 8$ deg. As the angle of attack increases, the different pitch rates converge and are nearly identical as early as 40 deg; the only exception to this is for the oscillatory behavior due to the vortex shedding that is present for K=1/64.
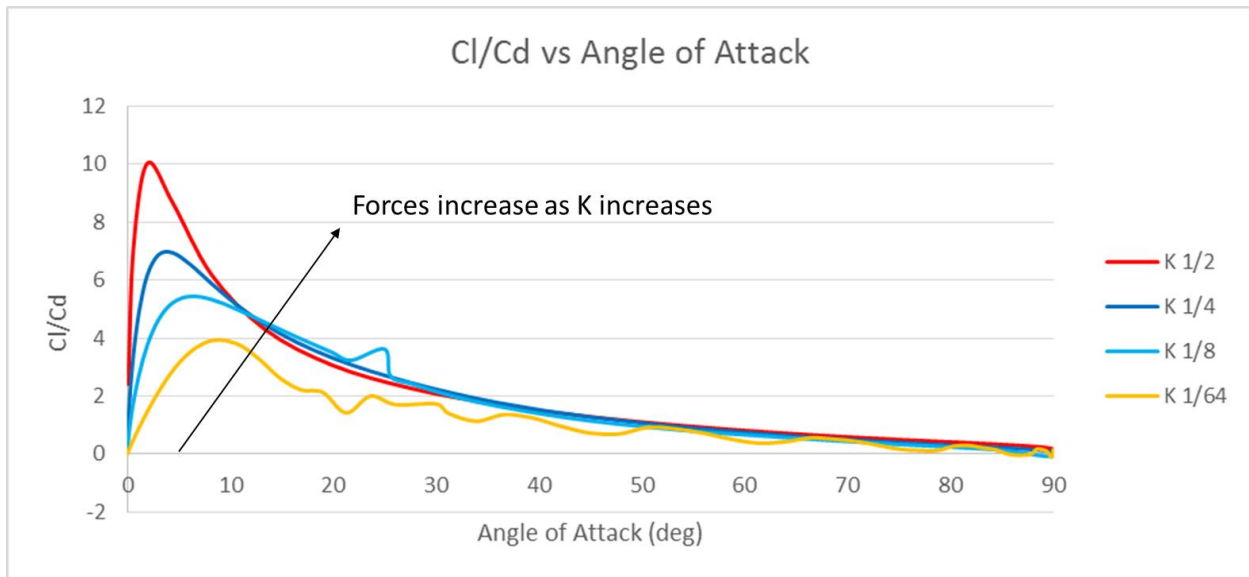
Figure 15: Lift over drag ratio as a function of α

III.2   Flow field for pitch rate at K = 1/2

Now I examine the details of the flow field for each pitch rate, by plotting the pressure, velocity vector, and vorticity fields. The case with K=1/2, i.e., the fastest pitch rate case, is discussed first. At this pitch rate, the airfoil would travel through a distance of two times chord length when it rotates from zero to 90 deg. It can be seen in Figure 16, that the pitch motion, or increasing the angle of attack, creates large velocity and pressure gradients around the airfoil. Looking at the pressure contour plots superimposed with velocity vectors, the figure shows that as the angle of attack increases, the stagnation point is located on the lower side of the airfoil and initially closer to the leading edge. Then, the stagnation point moves further away from the leading edge toward the trailing edge. This occurs due to the angle of attack exposing more of the lower surface to the freestream flow, creating effectively a larger cross-sectional area. Additionally, as the angle of attack increases, the difference in flow speed between the upper (or dorsal) and lower (ventral) surfaces increases significantly. This difference in the flow speed leads to pressure difference and lift generation. Alternatively, it can be seen in Figure 16 that as the angle of attack increases, the pressure on the upper surface drops drastically while the pressure on the lower surface decreases (at a slower rate). Also, it should be noticed that the region of lowest pressure on the upper surface occurs near the leading edge, which will cause more lift to be produced by the leading half of the airfoil than the trailing half. At α=54 and 77 deg., the low pressure zone above the airfoil is clearly more contracting toward the leading edge. On the other hand, separated low pressure regions have been developed in the wake away from the trailing edge. As shown later, such isolated low pressure zones correspond to vortices in the wake. Another observation is that the trailing edge stagnation point is not exactly located at the trailing edge for all four angles of attack shown, thus violating the steady Kutta condition that is in attached flow assumed by traditional aerodynamic theory. This Kutta condition break is consistent with what has been discussed previously by Polet (2015).

Figure 16: Pressure contour plot with velocity vectors for K= 1/2 at α= 25 (top left), 36 (top right), 54 (bottom left), and 77 (bottom right) deg.

The surface plots of the vorticity field around the airfoil are shown in Figure 17. The vorticity plot shows that initially the anticlockwise (red or positive) vorticity is along the entire ventral side as a shear layer and as the angle of attack increases, the anticlockwise shear layer moves further from the trailing edge and extends out further away from the airfoil. On the dorsal side, a negative (blue) shear layer is developed and is initially stably attached to the wing surface. Note that maximum lift occurs at α= 38 deg. At approximately 54 deg, separation of the shear layer on the dorsal side becomes visible and a clockwise leading vortex starts to be formed. As the angle of attack further increases, both the leading and trailing edge vortices grow in size while the leading edge vortex remains closer to the airfoil and has a larger velocity gradient than the trailing edge anticlockwise vortex. Flow separation is considered to be minimal for this rapid pitch-up maneuver.

Figure 17: Vorticity contour plot with velocity vectors for K= 1/2 at α= 25 (top left), 36(top right), 54 (bottom left), and 77 (bottom right) deg.

III.3   Flow field for pitch rate at K = 1/4

The pressure field arising for a pitch-up maneuver at a rate K= 1/4 is shown in Figure 18. At this pitch rate, the airfoil would travel through a distance of four times chord length when it rotates from zero to 90 deg. When comparing with the previous case of K=1/2, it can be seen that K=1/4 has similar pressure behavior in general, that is, a large low pressure zone on the dorsal side and a large high pressure zone on the ventral side. In addition, the low pressure zone corresponds to the leading-edge vortex being formed above the airfoil, and its shape evolves as the angle of attack increases. However, the difference between K=1/4 and K=1/2 cases is also evident. In particular, K=1/4 has more flow separation along the dorsal side of the airfoil at the same time moment. K=1/4 also produces less pressure difference between the dorsal and ventral sides; therefore, K=1/4 produces less lift than the previous case. Maximum lift occurs approximately at α=41 deg. and has much more flow separation at this maximum lift moment than that of K=1/2 in Figure 16 at its corresponding maximum lift.
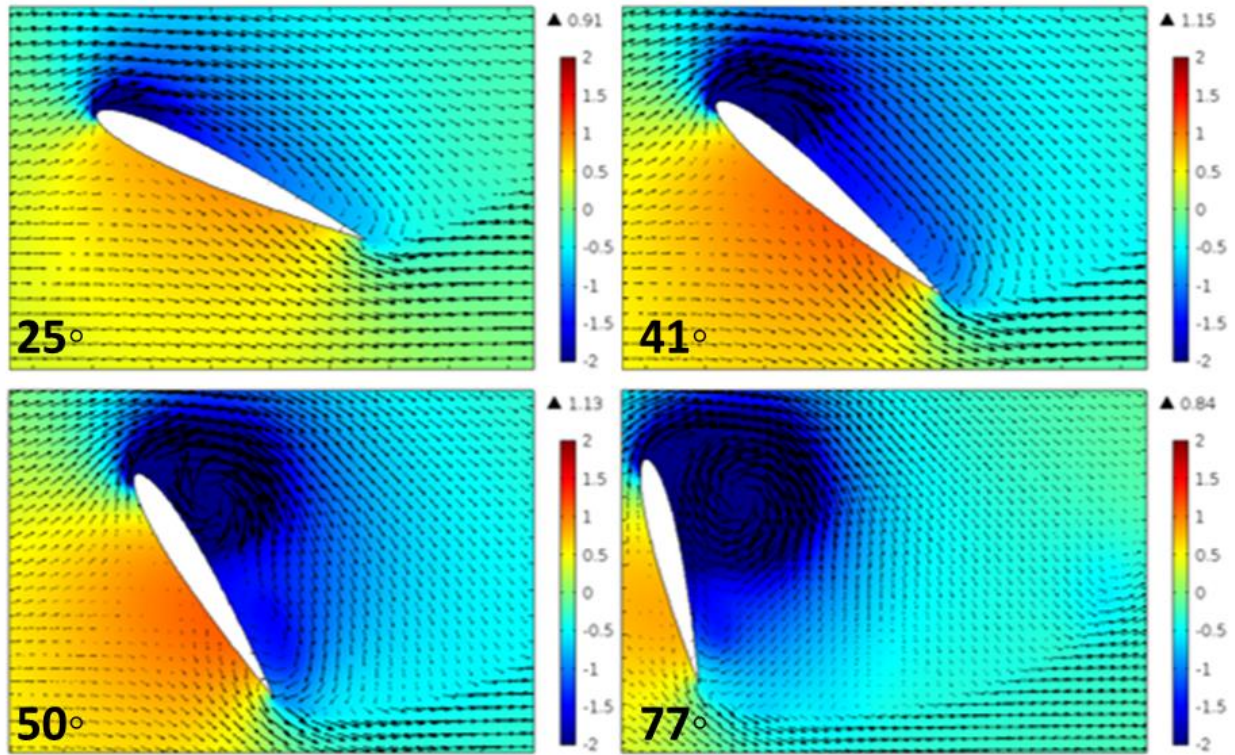
Figure 18: Pressure contour plot superimposed with velocity vectors for K= 1/4 at α= 25 (top left), 41 (top right), 50 (bottom left), and 77 (bottom right) deg.

When comparing the vorticity field of K=1/4 shown in Figure 19 with that of K=1/2 in Figure 17, the leading-edge vortex that forms with K=1/4 is larger in size, has less of a velocity gradient surrounding it, and is located further away from the airfoil. The trailing-edge vortex never seems to form as distinctly as it does for the faster pitch rate. Flow separation, as indicated by the vorticity, has increased and is easily visible at α=50 deg.

Figure 19: Vorticity contour plot superimposed with velocity vectors for K= 1/4 at α= 25 (top left), 41 (top right), 50 (bottom left), and 77 (bottom right) deg.

III.4   Flow field for pitch rate at K = 1/8

At this pitch rate, the airfoil would travel through a distance of eight times chord length when it rotates from zero to 90 deg. The pressure contour plots are illustrated in Figure 20. It can be seen that pressure difference between the two sides is again less than both of the previous pitch rates. Flow separation as indicated by the velocity field is actually visible as early as α=25 deg., and maximum lift occurs at α=43 deg. with significant flow separation along the leading edge of the airfoil.

When comparing the vorticity plot in Figure 21 with the previous two cases, a few noteworthy differences can be seen. Maximum lift occurs at 43 deg; two clockwise roll-up vortices are shown on the dorsal side, one near the leading edge and the other closer to the trailing edge; yet there isn't a clearly defined anticlockwise vortex until α=70 deg. At 70 deg., one large clockwise vortex is shown just behind the leading edge, and two to three much smaller anticlockwise vortices are downstream of the trailing edge.

28
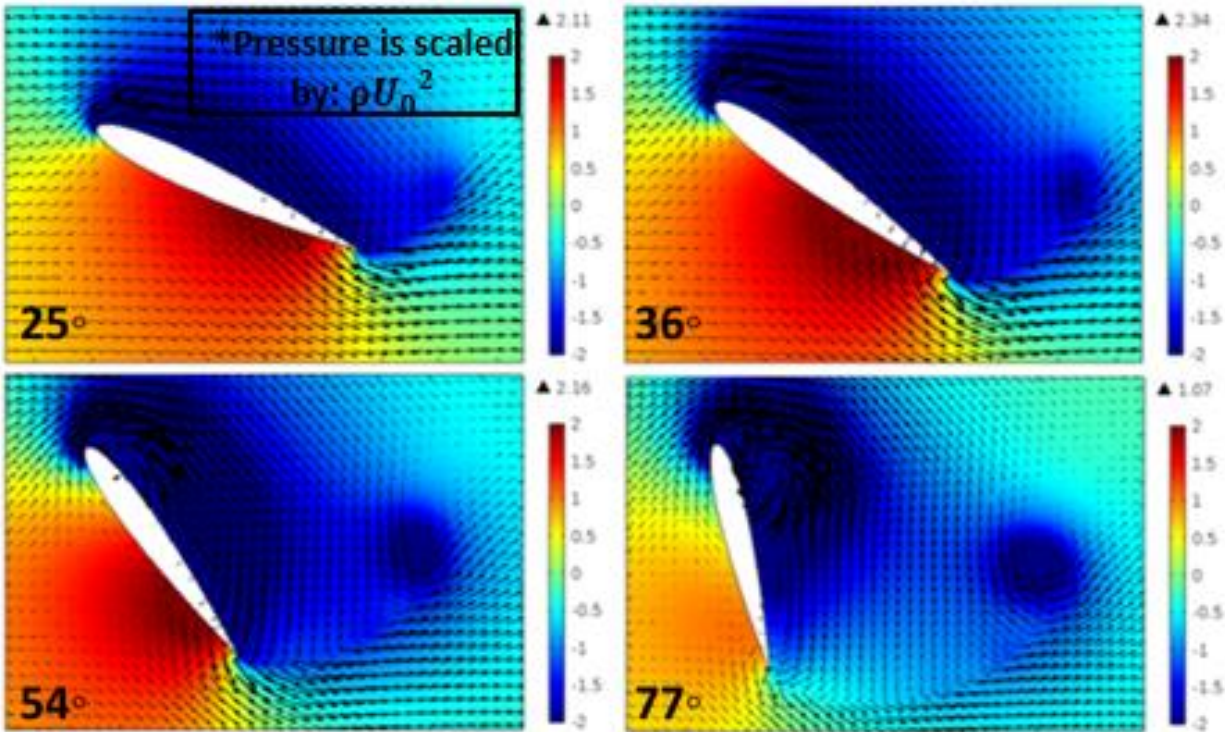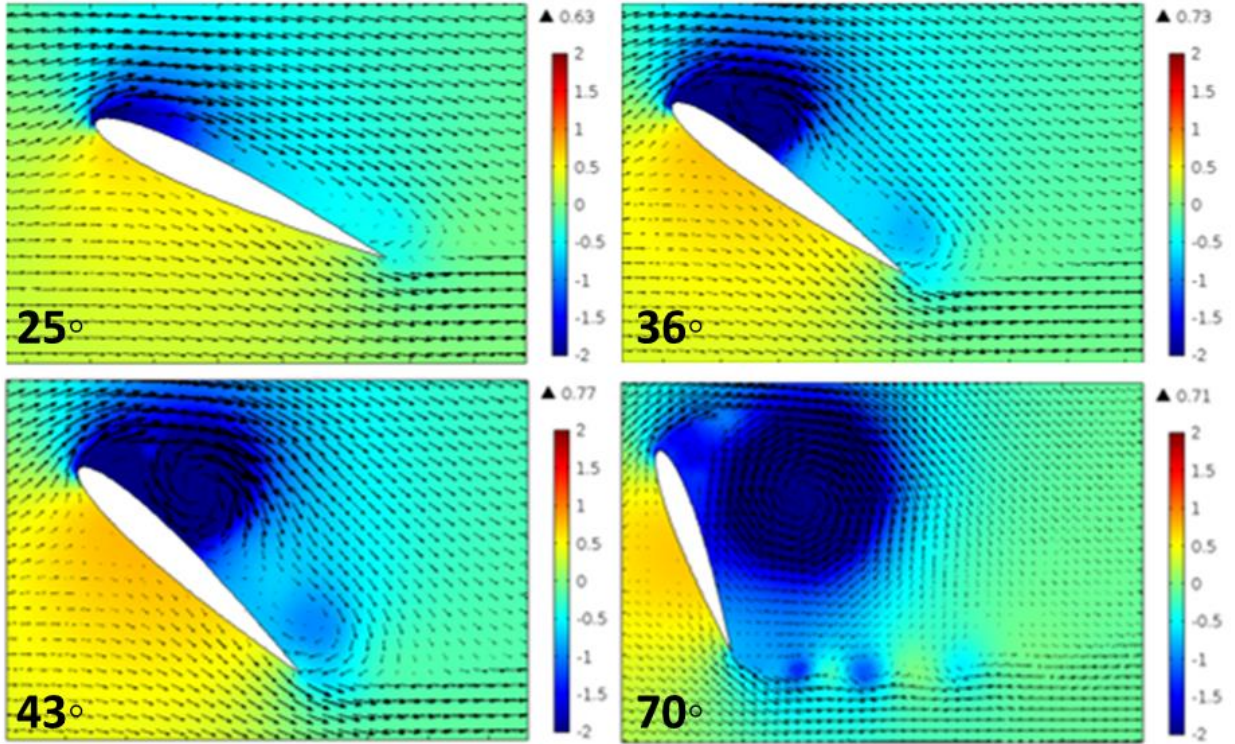
Figure 20: Pressure contour plot with velocity vector for K= 1/8 at α= 25 (top left), 36 (top right), 43 (bottom left), and 70 (bottom right) deg.
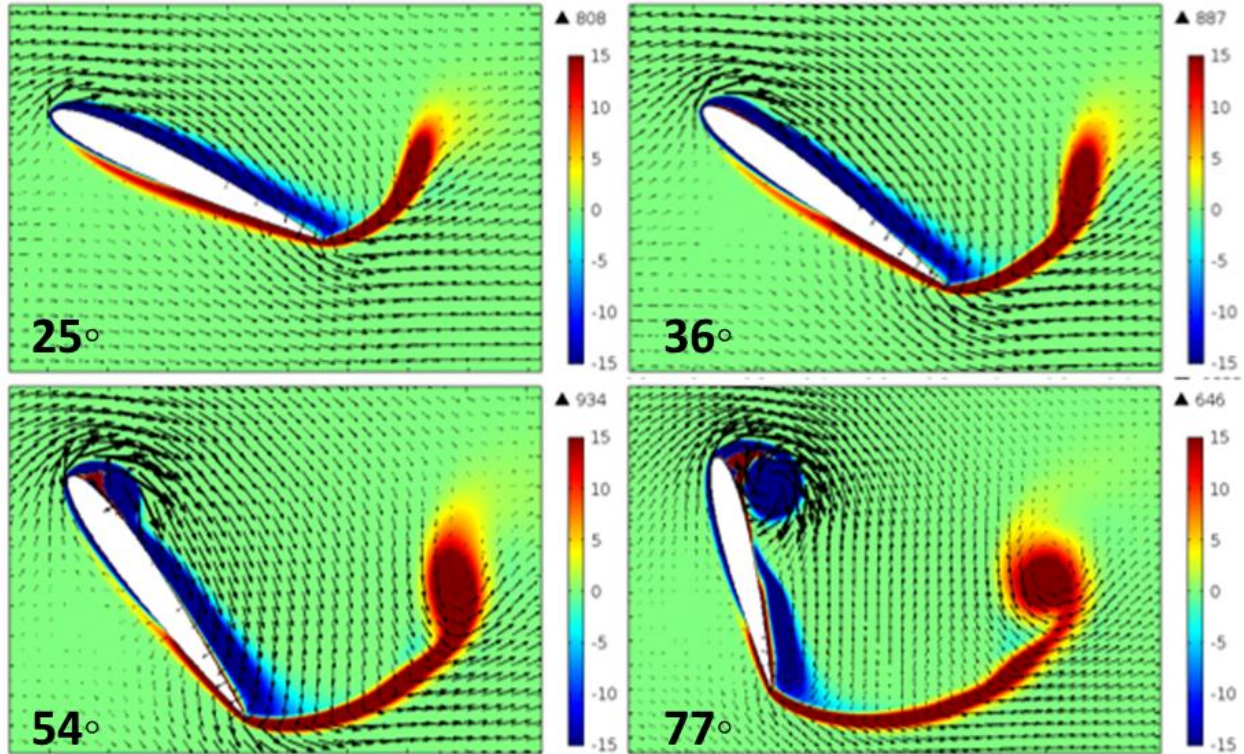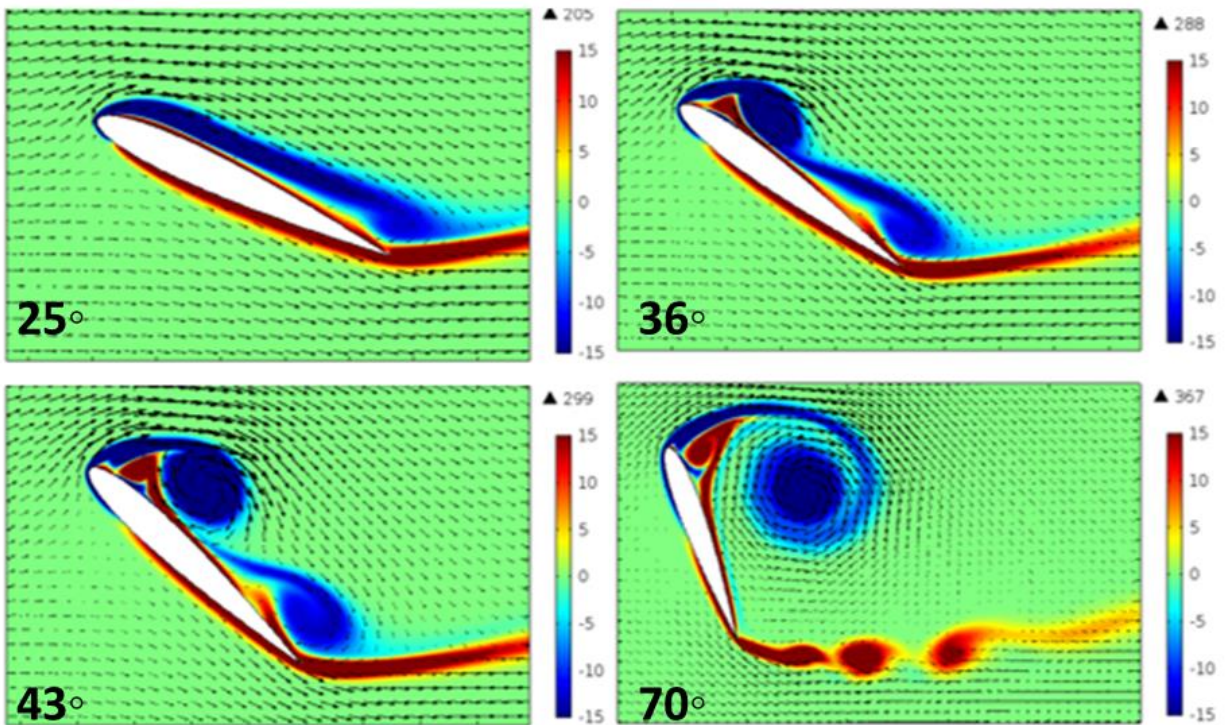
Figure 21: Vorticity contour plot with velocity vectors for K= 1/8 at α= 25 (top left), 36 (top right), 43 (bottom left), and 70 (bottom right) deg.

III.5   Flow field for pitch rate at K = 1/64

At this pitch rate, the airfoil would travel through a distance of 64 times of the chord length when it rotates from zero to 90 deg. The pressure field for this slowest pitch rate is shown below in Figure 22. Since the pitch rate is K=1/64, this should not be considered as a rapid pitch-up mauever and thefore will have significantly less rotational effects. As one might expect given the trend in the three previous pitch rates, flow separation is significantly worse than any of the previous cases, and the pressure difference between the two sides of the airfoil is even less. It's interesting to note that this was the only pressure field that resulted in two large low pressure zones downstream of the airfoil. In comparison, the previous pitch rates have only one large low pressure area.
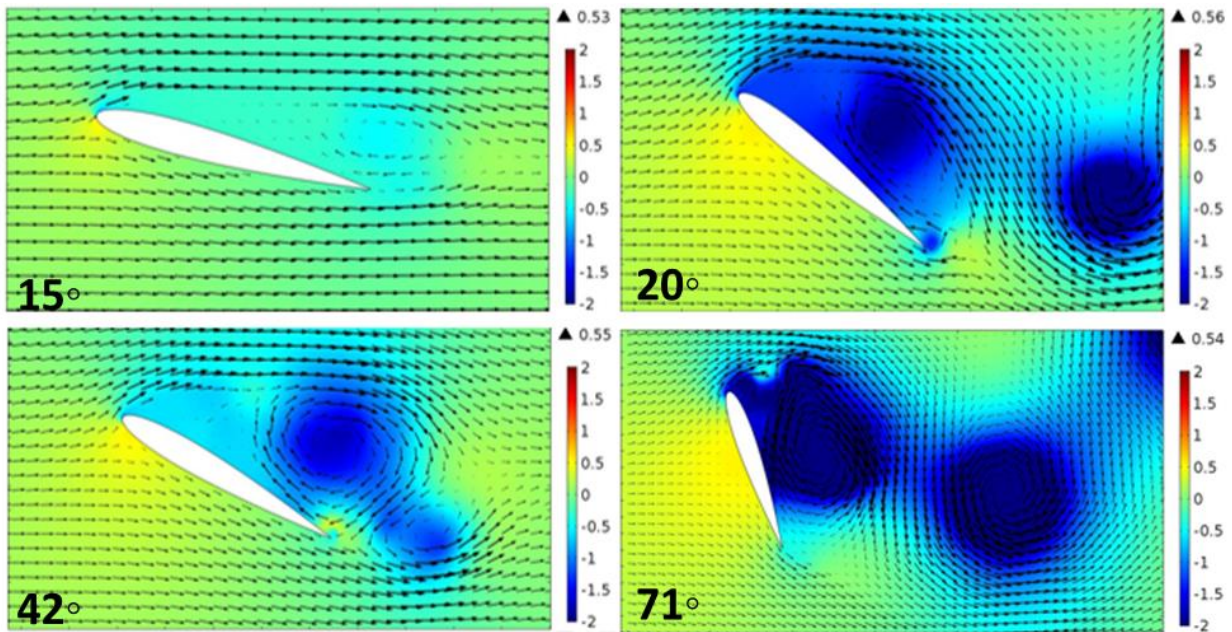
Figure 22: Pressure contour plot with velocity vector for K= 1/64 at α= 15 (top left), 20 (top right), 42 (bottom left), and 71 (bottom right) deg.

As mentioned earlier, the pitch rate is significantly slower than the previous cases and will have much lower inertial effects (in terms of flow attachment). Figure 23 shows that flow starts to separate from the dorsal surface as early as α=15 deg. Furthermore, this figure uniquely shows that the clockwise vortex that initially forms is located closer to the trailing edge than the leading edge. As the angle of attack increases, the clockwise vortex moves closer towards the leading edge of the airfoil. A single large anticlockwise vortex initially forms close to the tailing edge, but as the angle of attack increases, this positive vortex moves further downstream and pinches off from the trailing edge of the airfoil. Overall, the flow behaves like the unsteady flow would in the case of a stationary airfoil at the same angle of attack.
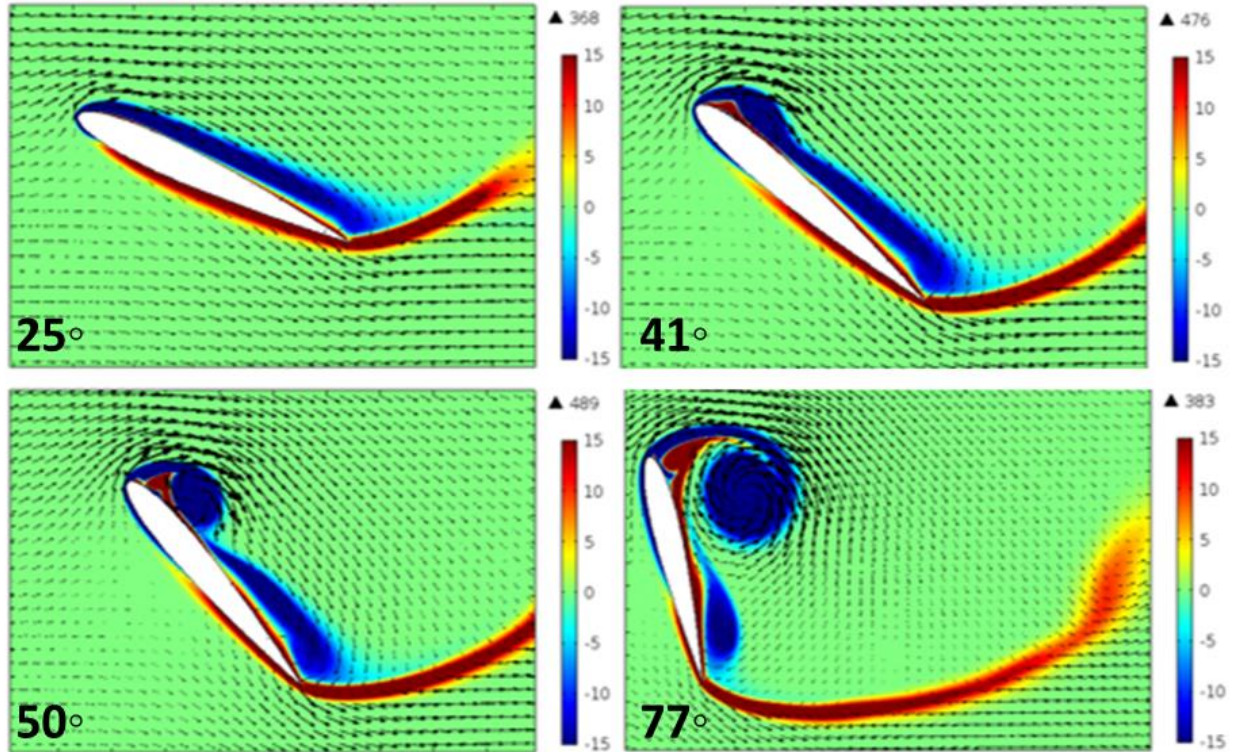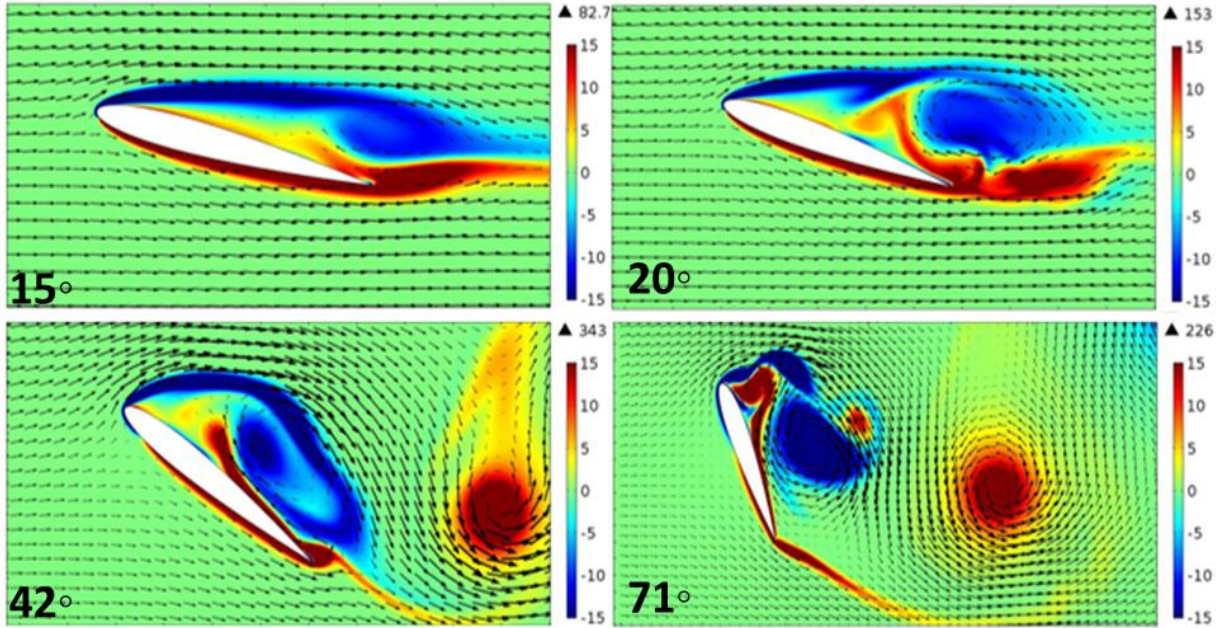
Figure 23: Vorticity contour plot with velocity vectors for K= 1/64 at α= 15 (top left), 20 (top right), 42 (bottom left), and 71 (bottom right) deg.

III.6   Discussion and conclusions

The study of the pitching wing has led to the following observations and conclusions.

First, the pitching rotation has very high impact on the temporary force production of the wing. From the four cases presented in this chapter, the peak lift increases by nearly four times as the pitch rate increases from K=1/64 to 1/2. Meanwhile, drag increase is also great (more than twice) when K increases from 1/64 to 1/2. These force spikes would be very useful for birds to perform highly controlled maneuvers. In particular, the high lift would allow a bird to maintain lift without significant stall while slowing down, and the high drag would help the bird to reduce its speed to come to stop.

Second, the pitching rotation enhances the force production of the wing by delaying boundary layer separation to a much higher angle of attack. From the present study, it is clear the faster the wings pitch, the more likely the boundary layer stays attached to the dorsal surface of the wing. Thus, the rapid pitching motion leads to an "inertial effect" of boundary layer stability and flow attachment. Leading edge vortex could be formed during the pitching process and also tends to remain attached to the wing if the pitch rate is fast enough.

Third, the leading-edge vortex formation corresponds to reattachment of the boundary layer, and the reattachment point moves toward the leading edge as the LEV evolves.

Fourth, the boundary layer separation, LEV formation, reattachment, and force production all seem to be nonlinear function of the pitch rate and instantaneous angle of attack and do not appear to be straightforward to describe using simple quantitative relationships.

Chapter IV   Unsteady aerodynamics of a perching airfoil

In this chapter, I will describe the results for an airfoil immersed in a uniform flow while performing the prescribed perching motion. That is, while it performs the pitch-up rotation, the wing also comes to stop with respect to the ambient air. I will discuss the force production, pressure distribution, vorticity field, and their dependence on pitch rate. The model setup, including the prescribed pitch rotation and linear translational velocity, computational domain, and mesh design, has been described in detail in Chapter II. The wing kinematics is the same as that in the validation case 1. In the present chapter, I use pitch rates at K=1/2, 1/4, 1/8, and 1/64 to perform a systematic study.

IV.1   Force production

The lift and drag forces are normalized in the same way as in previous chapters; that is, the initial translational velocity is used to define the lift and drag coefficients, despite that the airfoil translation is time-dependent in the perch maneuver. Before the perch maneuver starts, simulation has been performed to establish the initial flow field for the stationary airfoil at zero angle of attack.

The lift and drag forces generated by the NACA 0012 airfoil are shown below in Figure 24, it can be seen that as the pitch rate increases, so does the lift and drag that is produced. Comparing lift production with that in the previous chapter for pitching-only cases, the lift and drag forces are much lower for the present perching cases. This effect is understandable, as the freestream velocity, or the equivalent flight speed of the wing, is being reduced linearly as the angle of attack increases from zero to 90 deg. Nevertheless, despite the rapid flight speed drop, the force increase due to the pitching rotation is still quite impressive. As seen from this figure, the maximum lift at the fastest pitching, K=1/2, is nearly 10 times of that at the slowest pitching, K=1/64. Meanwhile, the maximum drag is also increased by 6 times, from Cd=0.5 to Cd=3.3. For a detailed comparison of these cases, I have tabulated the statistical data in Table 2.

In all cases, lift and drag have a similar trend: first increase and then decrease. However, the detailed force history has significant differences among these cases. Looking at the case of K=1/2, the lift peaks at approximately α=28 deg., while the drag doesn't peak until α=45 deg. As the pitch rate is decreased, maximum lift is delayed to a larger angle of attack, while maximum drag is slightly brought forward to a smaller angle of attack.

Comparing the different pitch rates, the Cl/Cd remains favorable until α= 53, 54, 51 and 47 deg. for pitch rates k= 1/2, 1/4, 1/8 and1/64, respectively. It is worth noting that like the pitching-only cases, neither the lift or drag peak at consistent times or angles across the different pitch rates, even though the prescribed angular velocity always has a maximum at α=45 deg. Figure 25 shows the angular velocity as a function of angle of attack.
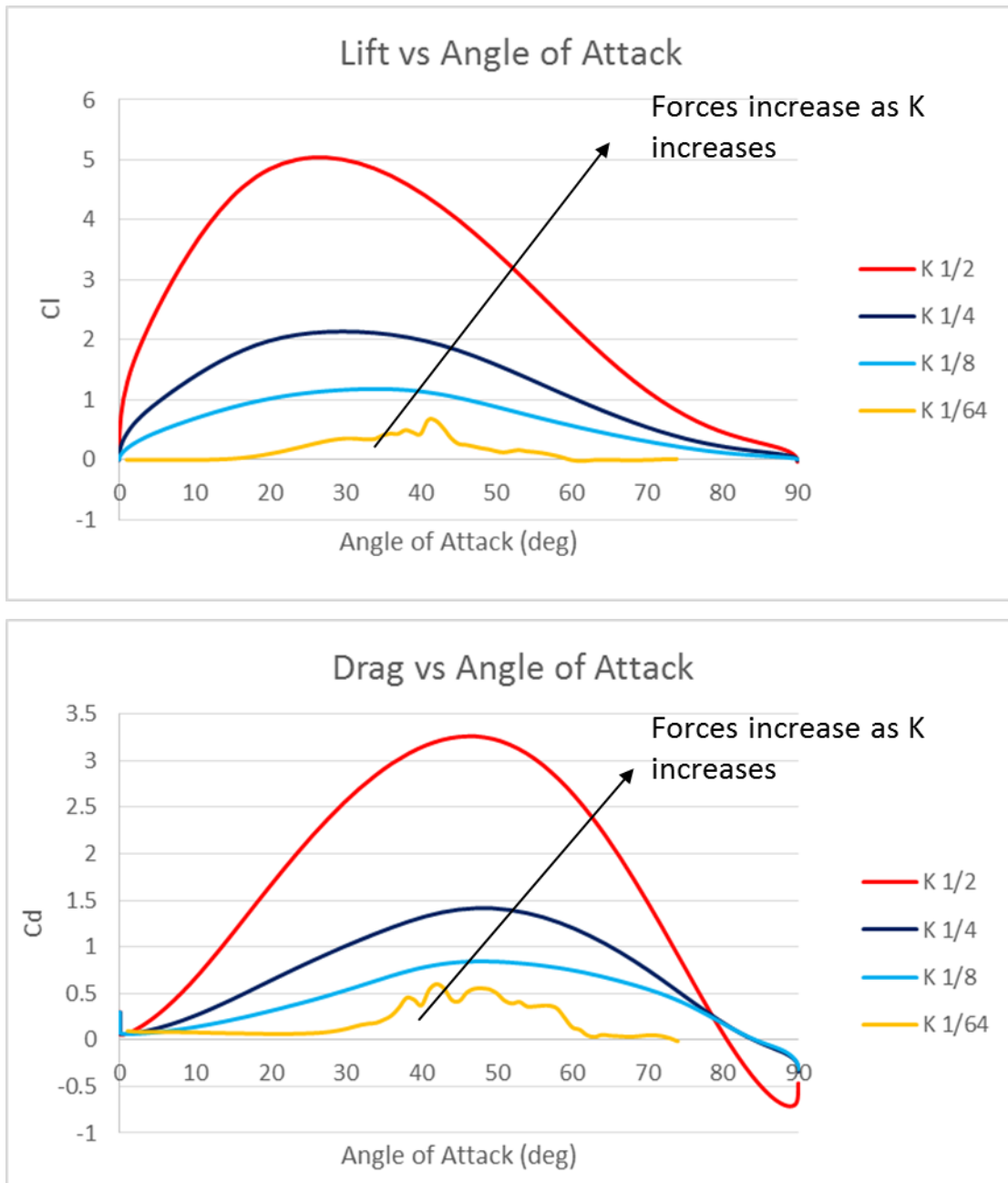
Figure 24: Lift (top) and drag (bottom) coeffcients as a function of angle of attack for K = 1/2, 1/4, 1/8 and 1/64.
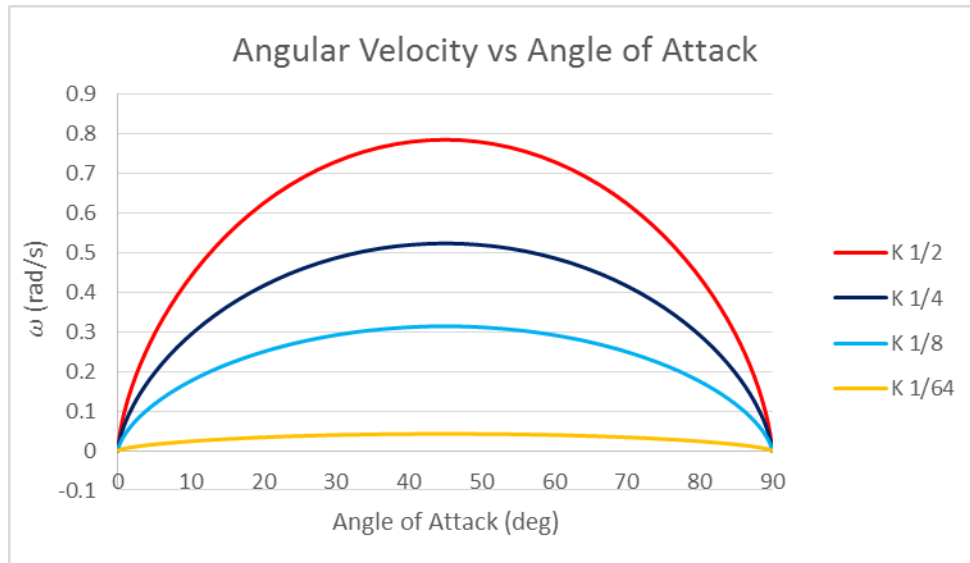
Figure 25: Prescribed angular velocity as a function of angle of attack for K = 1/2, 1/4, 1/8 and 1/64.

K	Max Cl at α		Max Cd at α		Max Cl/Cd at α		Avg Cl	Avg Cd	Avg Cl/Cd
1/2	5.04	27.58	3.26	45.00	17.46	1.12	1.96	0.83	2.35
1/4	2.14	29.64	1.42	47.25	8.25	2.99	0.82	0.40	2.08
1/8	1.18	33.89	0.84	48.37	5.44	5.64	0.43	0.23	1.87
1/64	0.66	42.19	0.60	45.00	3.71	9.65	0.18	0.21	0.84

Table 2: Detailed lift and drag statistics for the perching airfoil

The lift over drag ratio that was generated by the NACA 0012 airfoil is shown in Figure 26. As with pitching, the perching can be seen that as the pitch rate K increases, so do the peak lift over drag ratios that are produced at low angles of attack. As the pitch rate increases, the lift over drag peaks at a smaller α. Looking at fastest pitching at K=1/2, the lift over drag peaks at a Cl/Cd=17.46 at approximately $\alpha = 1$ deg. For K=1/4, 1/8, and 1/64, the lift over drag peaks are slightly delayed to larger angles of attack. Specifically, the peak lift over drag for K=1/4 is Cl/Cd = 8.25 at $\alpha = 3$ deg, for K=1/8 is Cl/Cd = 5.44 at $\alpha = 6$ deg, and for K=1/64 is Cl/Cd = 3.71 at $\alpha = 8$ deg. As the angle of attack increases, the different pitch rates converge and are nearly identical as early as 40 deg. Note that when finding the maximum Cl/Cd and discussing the trends, the oscillations at large angles of attack, $\alpha > 75$ deg, were ignored. At those angles of attack, the airfoil becomes nearly vertical. However, as it is slowing down, the fluid tracing the airfoil tends to maintain its momentum and thus pushes the airfoil from the dorsal side, leading to near zero or even negative drag seen in Figure 24. Corresponding, Cl/Cd could become very high, which is not very meaningful.
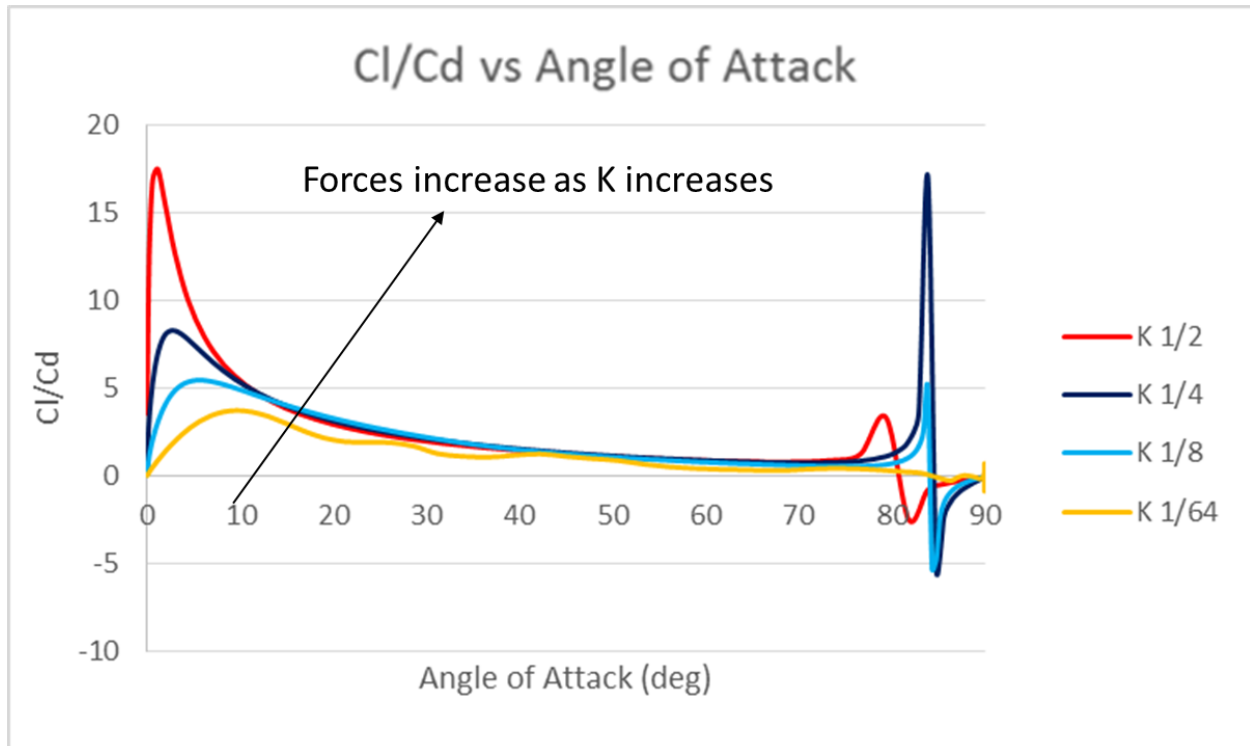
Figure 26: Lift over drag ratio as a function of angle of attack

IV.2   Flow field for pitch rate at K = 1/2

First, the fastest perching case with K=1/2 is examined. It can be seen in Figure 27 that increasing the angle of attack creates large velocity and pressure gradients around the airfoil. Looking at the pressure contour plots with velocity arrows, the figure shows that as the angle of attack increases, the stagnation point is initially located on the ventral side of the airfoil closer to the leading edge, and then the stagnation point moves toward to the trailing edge of the airfoil. This occurs due to the angle of attack exposing more of the ventral surface to the freestream flow and creating a larger cross-sectional area. Additionally, as the angle of attack increases the difference in flow speed between the distal and proximal surfaces increases significantly, this difference in velocity is what generates lift. Alternatively, Figure 27 shows that as the angle of attack increases, the pressure on the upper surface drops drastically while the pressure on the lower surface decreases (at a slower rate). The region of lowest pressure on the upper surface occurs near the leading edge, which will cause more lift to be produced by the leading half of the airfoil than the trailing half. At α=54 and 77 deg, low pressure vorticities are clearly present at the leading edge distal side. Note that the trailing edge stagnation point is not located at the trailing edge for all four angles of attack shown, thus violating the steady Kutta condition. This Kutta condition break is consistent with what has been discussed in Polet (2015). Comparing this perching rate with the corresponding pitching rate in Figure 16, it can be seen that the primary distinction between the two figures is that the pitching

36

case experienced a greater pressure differential between the dorsal and ventral sides of the airfoil and therefore the pitching case exhibits a stronger velocity gradient. The trailing edge vortex on the perching case remains closer to the airfoil at similar α's when compared with the pitching case.
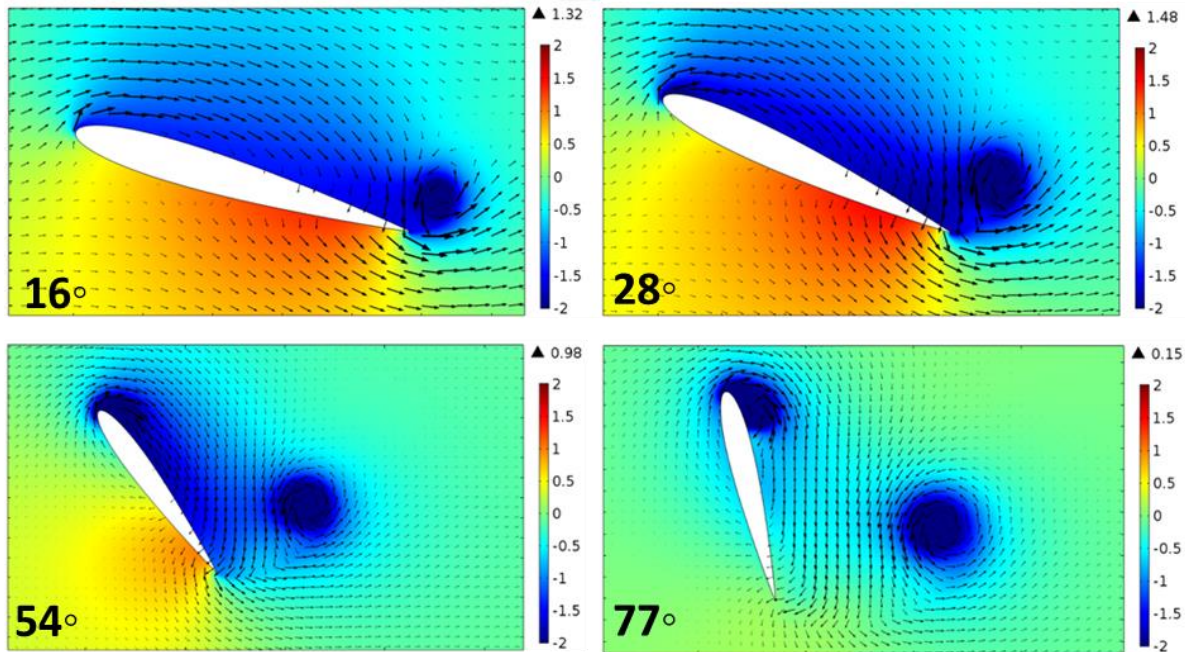
Figure 27: Pressure contour plot superimposed with velocity vectors for K= 1/2 at α= 16 (top left), 28 (top right), 54 (bottom left), and 77 (bottom right) deg.

The surface plots of the vorticity field around the airfoil is shown in Figure 28. The vorticity plot shows that initially the anticlockwise (red or positive) vorticity is along the entire ventral side as a shear layer and as the angle of attack increases, the anticlockwise shear layer moves further from the trailing edge and extends out further away from the airfoil. On the dorsal side, a clockwise (blue or negative) shear layer is developed and is initially stably attached to the wing surface. The maximum lift occurs at 28 deg. At approximately 54 deg separation of the shear layer on the dorsal side becomes visible and the clockwise leading vortex begins to take shape. As the angle of attack increases, both the leading and trailing edge vortices grow in size while the leading edge clockwise vortex remains closer to the airfoil and has a larger velocity gradient than the trailing edge anticlockwise vortex. Flow separation is considered to be minimal for this rapid perching maneuver. Comparing similar α's with the pitching case in Figure 17, the perching case not only shows a difference in the trailing edge vortex location but it shows a distinct difference in the shear layer on the dorsal side. For the perching case, the shear layer becomes detached midway along the airfoil where the shear layer remained along the airfoil for the pitching case for the entire pitch up maneuver.

Figure 28: Vorticity surface plot with velocity vectors for K=1/2 at α= 16 (top left), 28 (top right), 54(bottom left), and 77 (bottom right) deg

IV.3   Flow field for pitch rate at K = 1/4

The pressure field arising from a perching maneuver at a rate K=1/4 is shown in Figure 29. When comparing with the previous perching case of K=1/2, it can be seen that K=1/4 has similar pressure behavior in general, that is, a large low pressure zone on the dorsal side and a large high pressure zone on the ventral side. In addition, the low pressure zone corresponds to the leading-edge vortex being formed above the airfoil, and its shape evolves as the angle of attack increases. However, the difference between K=1/4 and K=1/2 cases is also evident. In particular, K=1/4 has more flow separation along the dorsal side of the airfoil at the same time moment. K=1/4 also produces less pressure difference between the dorsal and ventral sides; therefore, K=1/4 produces less lift than the previous case. Maximum lift occurs approximately at α=30 deg. and has much more flow separation at this maximum lift moment than that of K=1/2 in Figure 27 at its corresponding maximum lift. Another observation is that the trailing edge stagnation point is not exactly located at the trailing edge for all four angles of attack shown, thus violating the steady Kutta condition that is in attached flow assumed by traditional aerodynamic theory. Comparing this perching rate of K=1/4 with the corresponding pitching rate in Figure 18, it can be seen that the primary distinction between the two figures is that the pitching case experienced a significantly larger pressure differential between the dorsal and ventral sides of the airfoil and therefore the pitching case exhibits a corresponding stronger velocity gradient.

Figure 29: Pressure surface plot with velocity vectors for K=1/4 at α= 18 (top left), 30 (top right), 50 (bottom left), and 77 (bottom right) deg

When comparing the vorticity field in Figure 30 with Figure 28, the leading edge vortex that forms is larger in size, has less of a velocity gradient surrounding it and is located further away from the distal side of the airfoil. For this case, the trailing edge vortex has several smaller components compared to the faster pitch rate that produced one large vortex. Flow separation has increased and is easily visible at 50 deg. Comparing similar α's with the pitching case in Figure 19, several distinct differences can be observed. First, in the perching case, the shear layer on the dorsal side starts to detach from the airfoil surface at a lower angle of attack, and its leading edge vortex has slower development than in the pitching case. In addition, the trailing edge vortex tends to break up in the perching case, rather than forming a continuous sheet in the pitching case. These vortex behaviors appear to be related to the freestream flow speed that is slowing down in the perching case. This result suggests that in the perching case, the boundary layer has less inertia and is more prone to separation than in the pitching case.
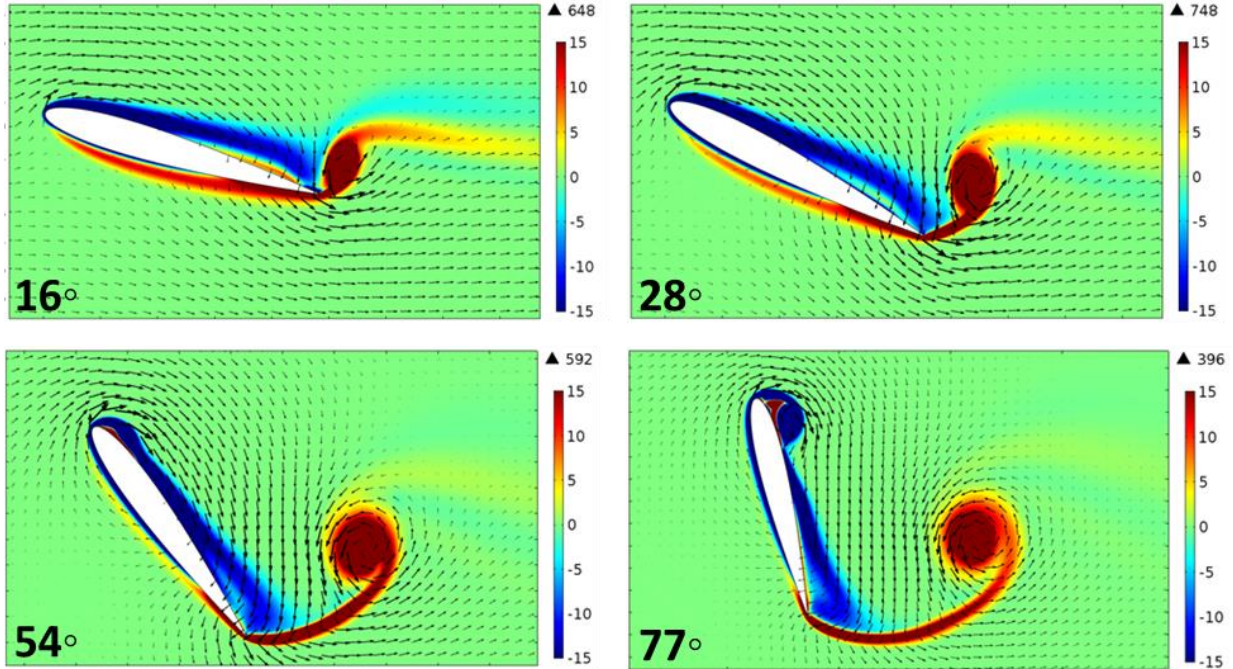
Figure 30: Vorticity surface plot with velocity vectors for K=1/4 at α= 18 (top left), 30 (top right), 50 (bottom left), and 77 (bottom right) deg

IV.4   Flow field for pitch rate at K = 1/8

The pressure field resulting from a perching maneuver at a rate K=1/8 is shown in Figure 31. When comparing with the previous faster perching cases (K=1/2 and 1/4), it can be seen that K=1/8 has similar pressure behavior in general, that is, a large low pressure zone on the dorsal side and a large high pressure zone on the ventral side. In addition, the low pressure zone corresponds to the leading-edge vortex being formed above the airfoil, and its shape evolves as the angle of attack increases. However, the key difference between K=1/8 and the faster perching cases is that K=1/8 has more flow separation along the dorsal side of the airfoil at the same time moment. Another observation is that the leading edge stagnation point is not exactly located at the leading edge for all four angles of attack shown, thus violating the steady Kutta condition that is in attached flow assumed by traditional aerodynamic theory. K=1/8 also produces less pressure difference between the dorsal and ventral sides; therefore, K=1/8 produces less lift than the previous cases. Maximum lift occurs approximately at α=34 deg. and has much more flow separation at this maximum lift moment than the faster perching cases at its corresponding maximum lift. Comparing this perching rate of K=1/8 with the corresponding pitching rate in Figure 20, it can be seen that the primary distinction between the two figures is that the pitching case experienced a significantly larger pressure differential between the dorsal and ventral sides of the airfoil and therefore the pitching case exhibits a corresponding stronger velocity gradient.
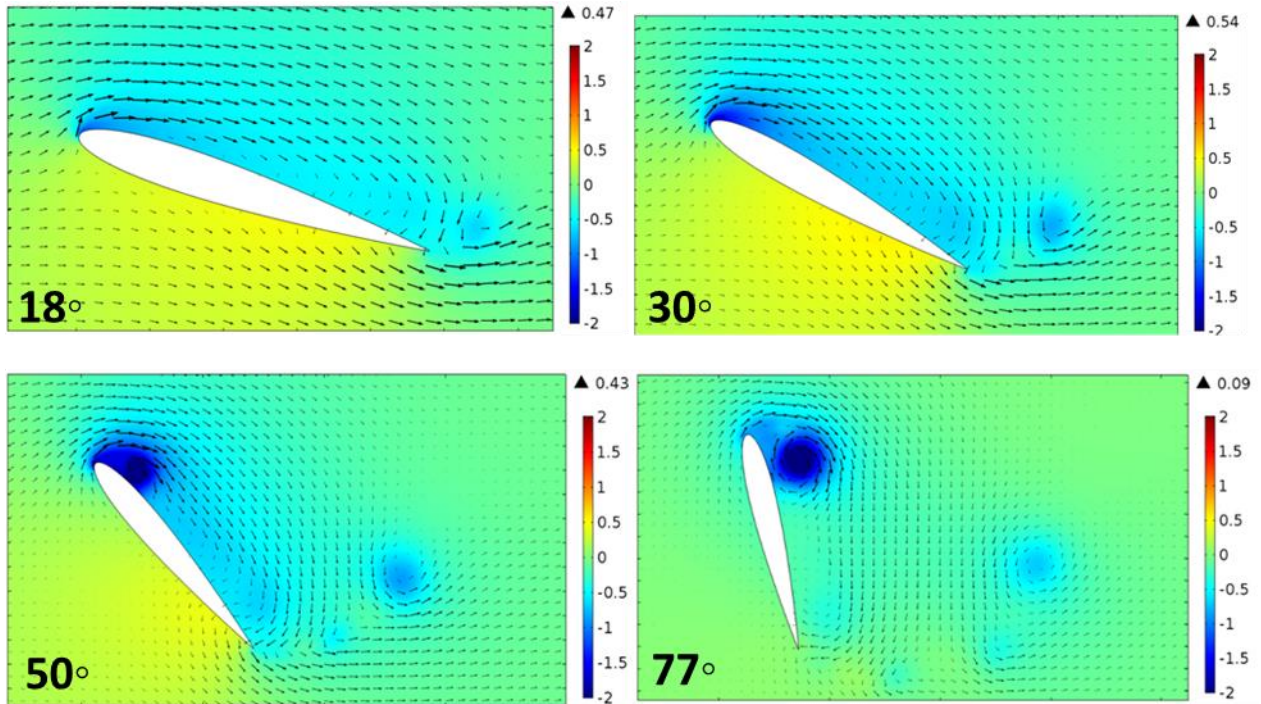
40
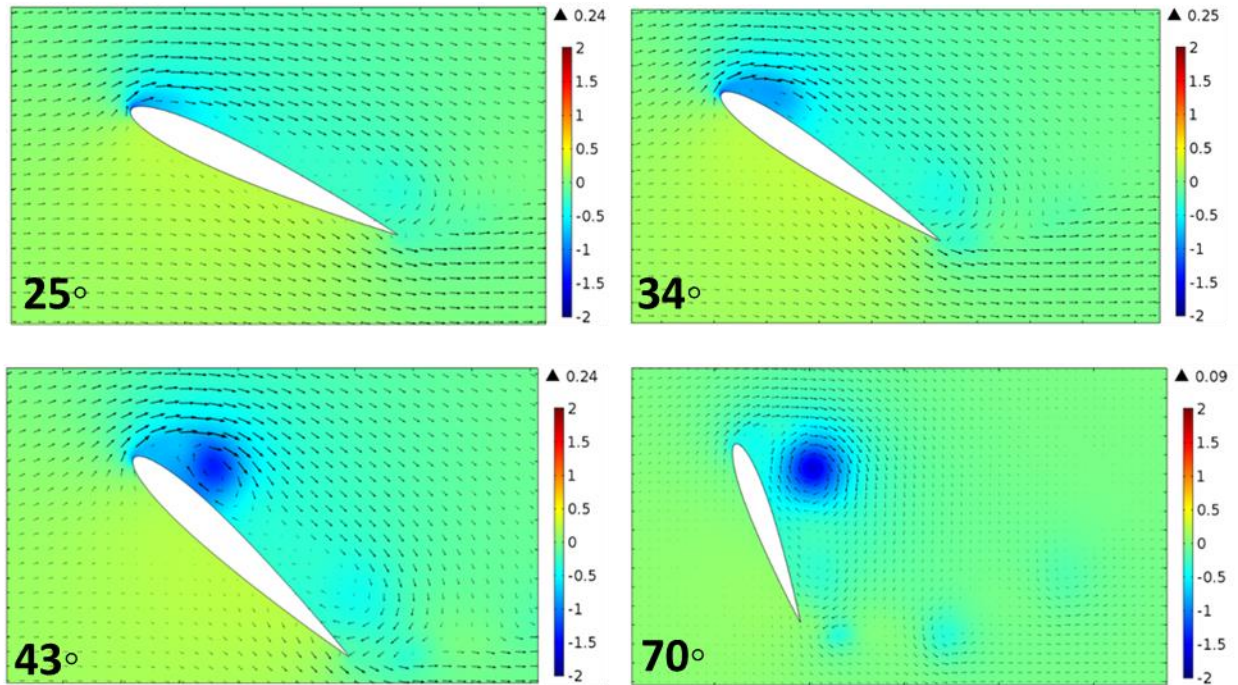
Figure 31: Pressure surface plot with velocity vectors for K=1/8 at α= 25 (top left), 34 (top right), 43(bottom left), and 70 (bottom right) deg

When comparing the vorticity field in Figure 32 with Figure 28 and Figure 30 , the leading edge vortex that forms is larger in size, has less of a velocity gradient surrounding it and is located further away from the distal side of the airfoil. For this case, the trailing edge vortex has several smaller components compared to the faster pitch rates. Flow separation has increased and is easily visible at 43 deg. At 70 deg, one large clockwise vortex is shown just behind the leading edge and three smaller anticlockwise vortices are located farther downstream of the trailing edge. Comparing similar α's with the pitching case in Figure 21, several distinct differences can be observed. Again, the boundary layer in the perching case tends to separate earlier than in the pitching case, and the leading edge vortex has much less development at similar angle of attack. The corresponding pitching case shows two clearly identifiable clockwise vortices present at 43 deg, a single clockwise vortex is located at each of the two ends of the airfoil. The perching case shows this similar second clockwise vortex but it isn't as cleanly defined. In addition, the trailing edge vortex has shorter extension and is less stable in the perching case.
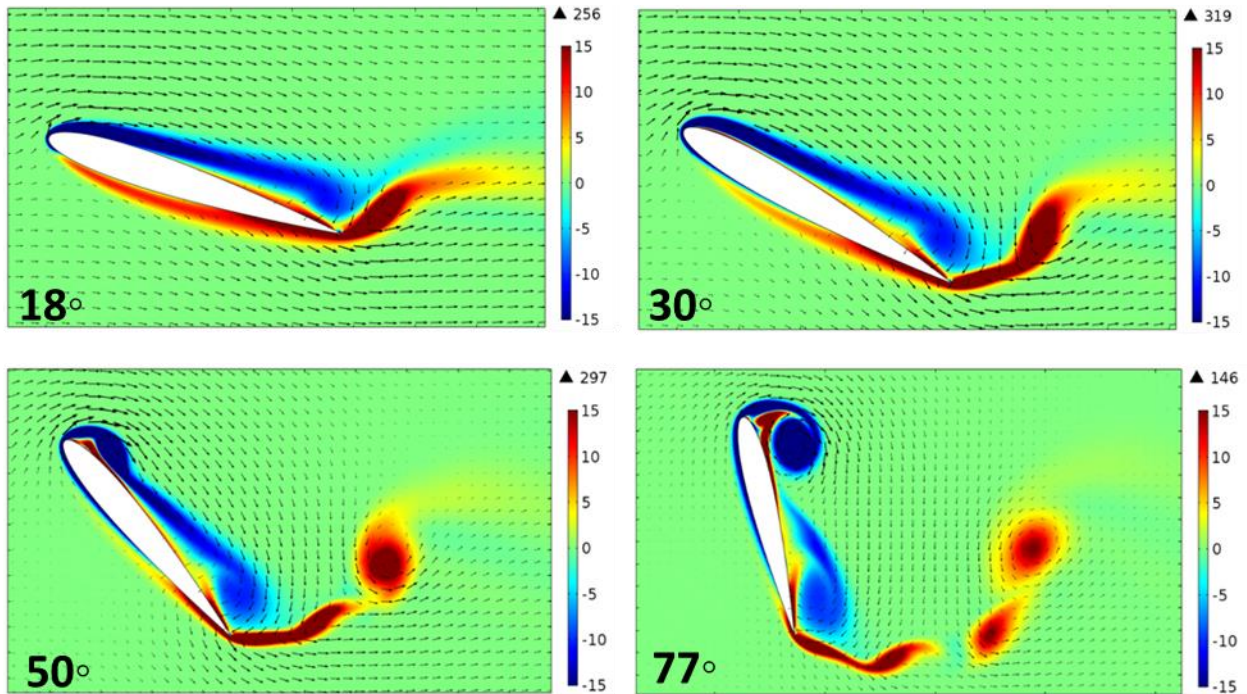
Figure 32: Vorticity surface plot with velocity vectors for K=1/8 at α= 25 (top left), 34 (top right), 43(bottom left), and 70 (bottom right) deg

IV.5   Flow field for pitch rate at K = 1/64

The pressure field for the slowest perching maneuver is shown in Figure 33. A perching maneuver at a rate K=1/64 shouldn't be considered a rapid pitch-up maneuver and therefore will have significantly less inertial effects. As one might expect, the dorsal side flow separation is significantly worse than any of the previous cases examined and occurs at a smaller α. The pressure differential between the dorsal and ventral sides of the airfoil is less than any of the other cases examined which results in the least amount of lift generated. A low pressure region is located near the trailing edge of the airfoil as early as 20 deg. Maximum lift occurs approximately at α=42 deg. When comparing this with the corresponding pitching case in Figure 22, the perching case again shows less of a pressure differential that was present during the pitching case.

42

Figure 33: Pressure surface plot with velocity vectors for K=1/64 at α= 15 (top left), 20 (top right), 42 (bottom left), and 71 (bottom right) deg

As mentioned earlier, the pitch rate is significantly slower than the previous cases and will have much lower inertial effects. Figure 34 shows that the clockwise vortex that initially forms is located closer to the trailing edge; whereas the previous perching cases showed the clockwise vortex forming at the leading edge. As α increases, the clockwise vortex moves closer towards the leading edge of the airfoil. A single large anticlockwise vortex initially forms close to the tailing edge, but as α increases the vortex moves further downstream away from the trailing edge of the airfoil. The shear layer detaches closer to the leading edge of the airfoil when compared with the previous perching cases. Comparing these results with the pitching case in Figure 23, both the leading shear layer and the trailing edge shear layer are much weaker in the perching case, so are the vortices in the wake.
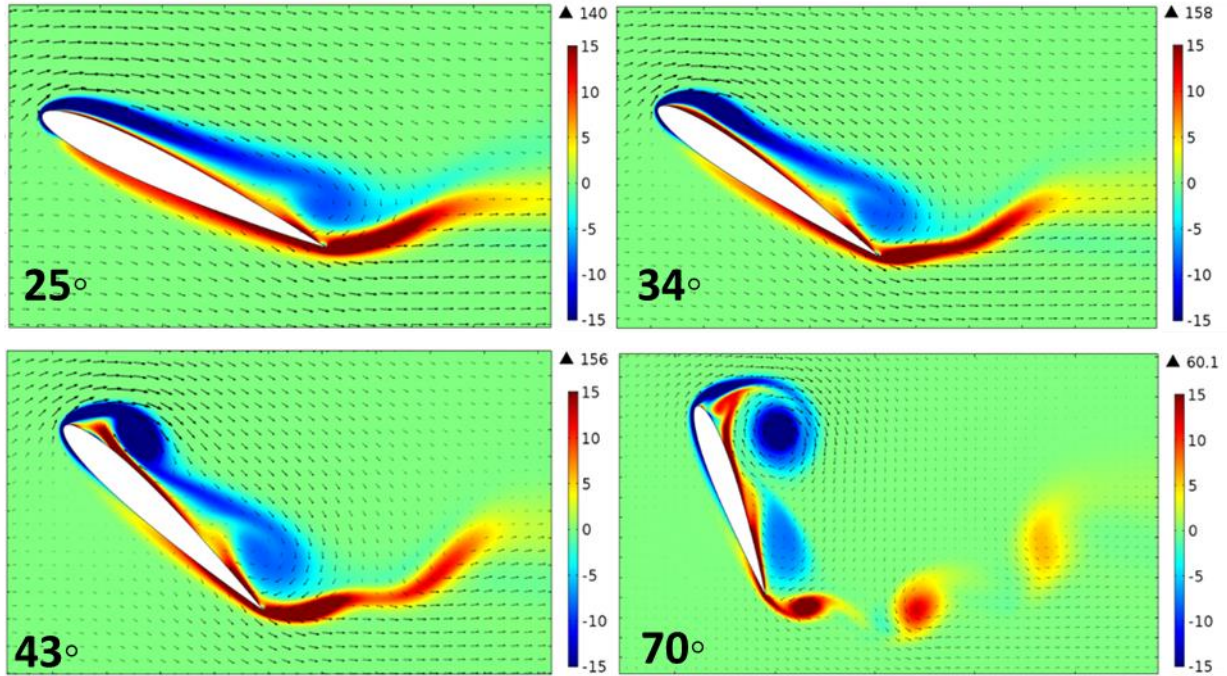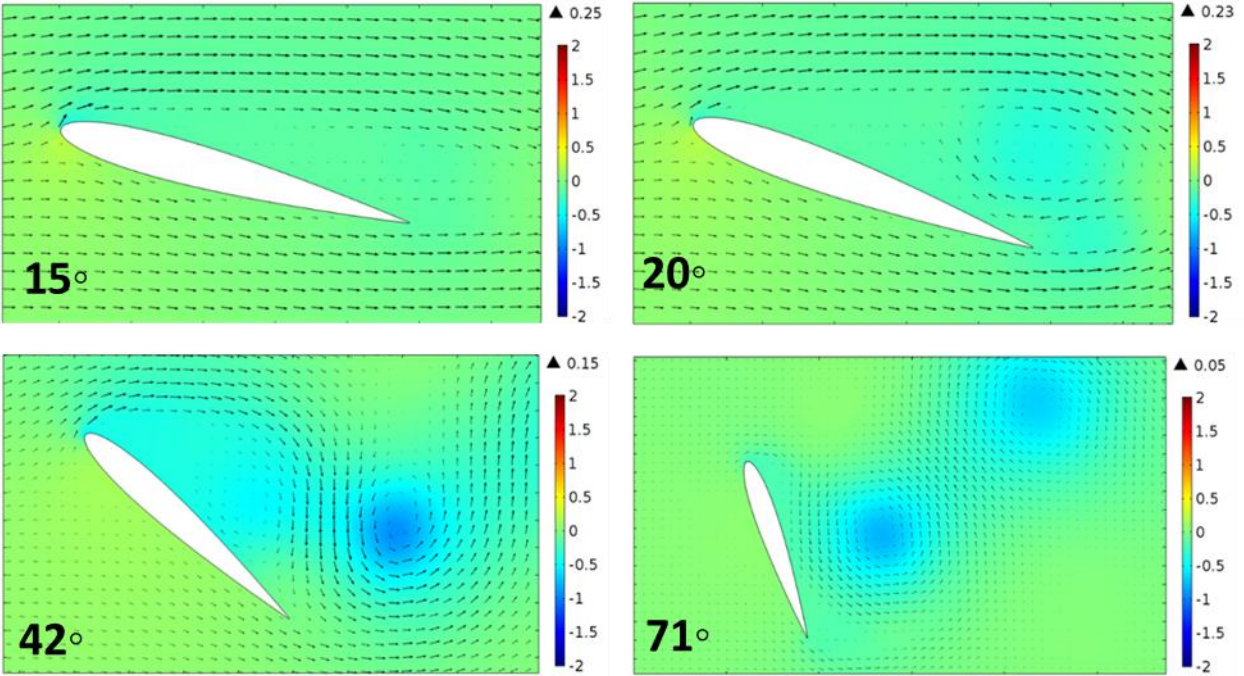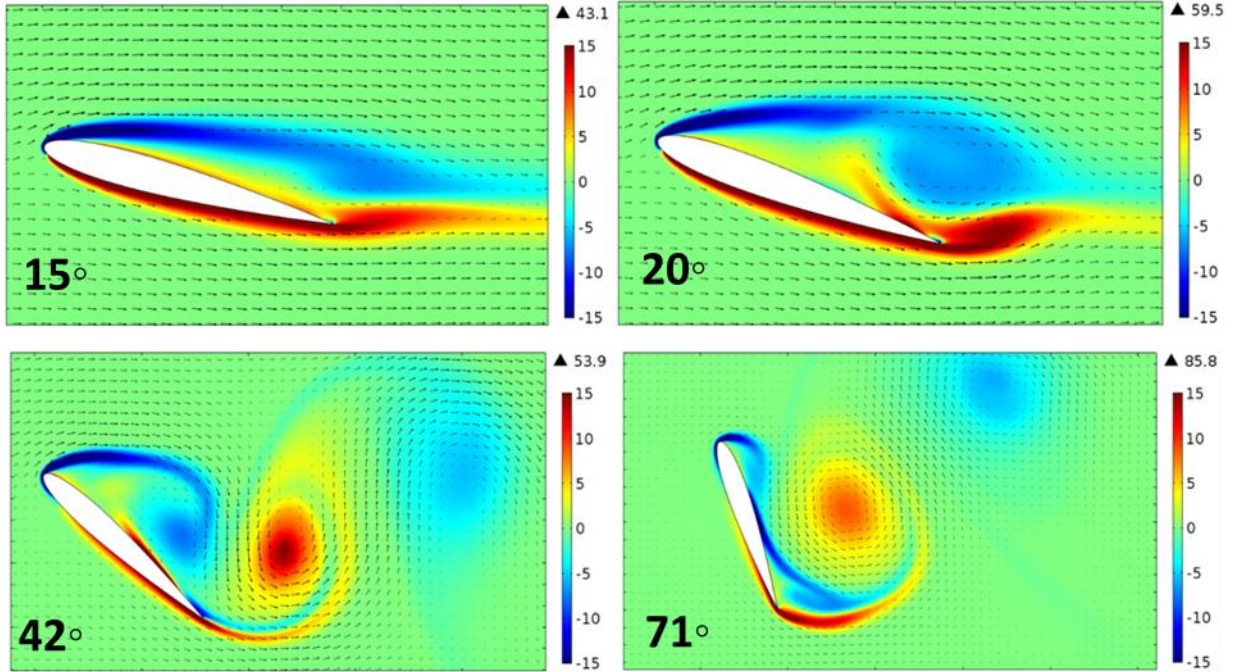
Figure 34: Vorticity surface plot with velocity vectors for K=1/64 at α= 15 (top left), 20 (top right), 42 (bottom left), and 71 (bottom right) deg

IV.6   Discussions and conclusions

The study of the perching wing has led to the following observations and conclusions.

First, like in the pitching maneuver, the pitch-up rotation in the perching maneuver also has very high impact on the temporary force production of the wing. The force enhancement by fast perching is very impressive, even though the overall force production of wing is much lower as compared with pitching maneuver where the flight speed remains constant. From the four cases presented in this chapter, the peak lift increases by nearly eight times as the pitch rate increases from K=1/64 to 1/2. Meanwhile, drag increase is also great (more than five times) when K increases from 1/64 to 1/2. Therefore, the force enhancement from slow perching to fast perching is even greater than in the corresponding cases in pitching maneuver. These force spikes would be very useful for birds to perform highly controlled maneuvers and in fact might be critical for birds during perching maneuver where the slow flight speed alone is likely not sufficient to provide enough lift or drag. The present study thus confirms the significant role of pitch rotation in aerodynamics of perching maneuver.

Second, like in the pitching maneuver, the pitch-up rotation enhances force production of the wing by delaying boundary layer separation to a much higher angle of attack. From the present study, it is clear the faster the wings pitch, the more likely the boundary layer stays attached to the dorsal surface of the wing. Thus, the rapid pitching motion also leads to an "inertial effect" of boundary layer stability and flow attachment in the current situation, where the relative speed of air with respect to the wing drops quickly. Like the pitching wing, a leading edge vortex could be formed

44

during the pitching process and also tends to remain attached to the wing if the pitching rate is fast enough. Compared with the pitching wing, the inertial effect of the boundary layer and leading edge vortex are not as strong in the perching case. However, they still correlate strong with the force enhancement introduced by the wing rotation.

Finally, the boundary layer separation, LEV formation, reattachment, and force production all seem to be nonlinear function of the pitch rate and instantaneous angle of attack and do not appear to be straightforward to describe using simple quantitative relationship.

Chapter V Conclusions and future study

In this work the force production, pressure distribution, and vorticity field were investigated in a controlled pitch-up maneuver. For simplicity, NACA 0012 airfoil was utilized, and a variety of pitch rates ranging from 1/64 to 1/2 were used to accurately describe force production in relation with the wing velocity, acceleration, rotational velocity, and rotational acceleration. This work investigated how the wing-pitching affects the force production, boundary layer detachment, and vortex formation in the flow.

Two validation cases were carried out to verify this study's model setup and assess the accuracy of COMOSL's simulation. In the first validation study, the perching maneuver kinematics specified by Polet et al (Polet et al., 2015) were compared. The simulated vorticity fields presented in this study agrees with the simulated vorticity fields and the particle image velocimetry measurements that Polet et al (Polet et al., 2015) acquired. These results demonstrated the same wake features, vorticity magnitudes, and force production which builds confidence in this study.

A second validation case was considered, where two different types of translational motion were considered, first pitching where U(t)= U_0 (i.e., constant speed) and the second case, perching which is defined by Granlund et al (2010), where the wing decelerates linearly until rest during the pitch-up maneuver. The case was numerically studied by Wang and Eldredge (2012) using a highly accurate viscous vortex particle method. The simulated vorticity fields, force production, and wake features presented in this study are consistent with those in the Wang and Eldredge (2012) which further establishes confidence in this study. The pitching wing showed that the pitching rotation significantly impacts the temporary force production of the wing. As the pitch rate increases from 1/64 to 1/2, the peak lift and drag increase by nearly four and more than two times respectievely. For all four pitch rates examined, the lift peaks considerably sooner during the pitch-up maneuver than the drag force. In addition, the pitching rotation augments the force production of the wing by delaying the boundary layer separation to a higher angle of attack. As the pitch rate increases, the boundary layer is more likely to stay attached to the dorsal surface of the wing for a longer duration of the pitch-up manuever. This rapid pitching motion results in an "inertial effect" of boundary layer stability and flow attachment. The leading-edge vortex formation corresponds to the reattachment of the boundary layer, and the reattachment point moves closer towards the leading edge of the wing as the LEV evolves throughout this pitch-up manuever. The force spikes, delayed boundary layer separation and LEV would be very useful for birds performing highly controlled manuevers such as landing on a narrow platform in tight corridors. The high lift would allow a bird to maintain lift, the delayed boundary layer separation would prevent the bird from stalling while slowing down, and the high drag would help the bird to reduce its speed when coming to a stop.

Similarly to the pitching wing, the perching wing's pitch-up rotation substantially influences the temporary force production of the wing. The fast perching force enhancement is considered signifcant, even though the overall force production of the wing is much lower than force production during the pitching maneuver where the flight speed remains constant. As the pitch rate increases from 1/64 to 1/2, the peak lift and drag increase by nearly eight and more than five times respectievely.Therefore, the force enhancement from slow perching to fast perching is even greater

than in the correspoinding cases in pitching maneuver. The force spikes would be very useful for birds to perform highly controlled maneuvers and in fact might be critical for birds during perching maneuver where the slow flight speed alone is likely not sufficient to provide enough lift or drag. The present study thus confirms the significant role of pitch rotation in aerodynamics of perching maneuver. Again, as the pitching rotation increases, the force production of the wing increases by delaying the boundary layer separation to a higher angle of attack. This rapid pitching motion results in an "inertial effect" of boundary layer stability and flow attachment. The leading-edge vortex formation corresponds to the reattachment of the boundary layer, and the reattachment point moves closer towards the leading edge of the wing as the LEV evolves throughout this pitch-up manuever. The inertial effect of the boundary layer and leading edge vortex presented in this stufy for perching were not as strong as for the pitching case. However, they still correlate strong with the force enhancement introduced by the wing rotation.The force spikes, delayed boundary layer separation and LEV would be essential for birds attempting the perching maneuver.

Both the pitching and perching cases showed that the boundary layer separation, LEV formation, reattachment, and force production all seem to be nonlinear functions of the pitch rate and instantaneous angle of attack and do not appear to be straightforward to describe using simple quantitative relationship.

For the future study, one possible extension of the current study is to investigate the corresponding three-dimensional situations. For that purpose, either a translating or pitching airfoil with a finite aspect ratio, or a revolving-pitching wing with non-uniform wing velocity along the span, could be considered. It would be interesting to see how the pitching motion enhances the shear layer attachment and leading edge vortex stability in the three-dimensional context.

REFERENCES

Angeles, L., & Angeles, L. (2010). On the roles of chord-wise flexibility in a flapping wing with hovering kinematics, *Journal of Fluid Mechanics, Volume 659*, 94–115. http://doi.org/10.1017/S0022112010002363

Carruthers, A. C., Thomas, A. L. R., & Taylor, G. K. (2007). Automatic aeroelastic devices in the wings of a steppe eagle Aquila nipalensis. *The Journal of Experimental Biology*, *210*(Pt 23), 4136–4149. http://doi.org/10.1242/jeb.011197

Cory, R., Tedrake, R. (2008). Experiments in Fixed-Wing UAV Perching. *AIAA Guidance Navigation and Control Conference and Exhibit*, AIAA 2008-7256. http://doi.org/10.2514/6.2008-7256

Dai, H., Luo, H., & Doyle, J. F. (2012). Dynamic pitching of an elastic rectangular wing in hovering motion. *Journal of Fluid Mechanics, Volume 693, 473-899*

Dickinson, M. H., Lehmann, F., & Sane, S. P. (1999). Wing Rotation and the Aerodynamic Basis of Insect Flight. *Science* 18 Jun 1999, Vol. 284, Issue 5422, pp 1954-1960.

Dudley, B. Y. R., & Ellington, C. P. (1990a). Mechanics of Forward Flight in Bumblebees, *Journal of Experimental Biology 1990 148: 19-52*

Dudley, B. Y. R., & Ellington, C. P. (1990b). Mechanics of Forward Flight in Bumblebees, *Journal of Experimental Biology 1990 148: 53-88*.

Granlund, K., Ol, M., Garmann, D., & Visbal, M. (2010). Experiments and Computations on Abstractions of Perching. *28th AIAA Applied Aerodynamics Conference*, (July), AIAA 2010-4943, 4943.

Hedenstro, A., & Johansson, L. C. (2015). Bat flight : aerodynamics , kinematics and flight morphology, *Journal of Experimental* Biology 2015 218:653-663. http://doi.org/10.1242/jeb.031203

Liu, H., & Kawachi, K. (1998). A Numerical Study of Insect Flight, *Journal of Computational Physics,* Volume 146, Issue *1156*, 124–156.

Ortega-jimenez, V. M., Greeter, J. S. M., Mittal, R., & Hedrick, T. L. (2013). Hawkmoth flight stability in turbulent vortex streets, *Journal of Experimental* Biology 2013 216:4567-4579. . http://doi.org/10.1242/jeb.089672

Pesavento, U., & Wang, Z. J. (2009). Flapping wing flight can save aerodynamic power compared to steady flight. *Physical Review Letters*, *103*(11). http://doi.org/10.1103/PhysRevLett.103.118102

Peskin, C. S., & Dora, T. (2002). The immersed boundary method. *Acta Numerica*, 479–517. http://doi.org/10.1017/S0962492902000077

Polet, D. T., Rival, D. E., & Weymouth, G. D. (2015). Unsteady dynamics of rapid perching manoeuvres. *Journal of Fluid Mechanics*, *767,* (2014), 323–341. http://doi.org/DOI 10.1017/jfm.2015.61

Song, J. (2016). Computatiional Modeling of Unsteady Aerodynamcics in Hummingbird Flight. Vanderbilt University, 2016-01-11, etd-01192016-100906

Song J, Luo H, Hedrick TL. 2014 Three-dimensional flow and lift characteristics of a hovering ruby-throated hummingbird. J. R. Soc. Interface 11: 20140541. http://dx.doi.org/10.1098/rsif.2014.0541

Spedding, G. R., Rosén, M., & Hedenström, A. (2003). A family of vortex wakes generated by a thrush nightingale in free flight in a wind tunnel over its entire natural range of flight speeds *Journal of Experimental Biology,* 206:2313-2344, http://doi.org/10.1242/jeb.00423

Sun, M., & Tang, J. (2002). Unsteady aerodynamic force generation by a model fruit fly wing in flapping motion, *Journal of Experimental Biology, 205:55-70*.

Tobalske, B. W., Warrick, D. R., Clark, C. J., Powers, D. R., Hedrick, T. L., Hyder, G. A., Biewener, A. A., (2007). Three-dimensional kinematics of hummingbird flight, *Journal of Experimental Biology,* 210:2368-2382. http://doi.org/10.1242/jeb.005686

Wang, C., & Eldredge, J. D. (2012). Low-order phenomenological modeling of leading-edge vortex formation. *Theoretical and Computational Fluid Dynamics*, 1–22. http://doi.org/10.1007/s00162-012-0279-5

Wang, Z. J. (2005). Dissecting insect flight, *Fluid Mech, 34:183-210*. http://doi.org/10.1146/annurev.fluid.36.050802.121940

Wang, Z. J., Birch, J. M., & Dickinson, M. H. (2004). Unsteady forces and flows in low Reynolds number hovering flight : two-dimensional computations vs robotic wing experiments, *Journal of Experimental Biology,* 207: 449–460. http://doi.org/10.1242/jeb.00739

Yin, B., & Luo, H. (2010). Effect of wing inertia on hovering performance of flexible flapping wings, *Physics of Fluids,* 22, 111902, 1–10. http://doi.org/10.1063/1.3499739

Zhao, J., He, C., Zhang, L., Zhao, H., & Hu, P. (n.d.). Coupled Viscous Vortex Particle Method and Unstructured Computational Fluid Dynamics Solver for Rotorcraft Aerodynamic Interaction Analysis. 49th *AIAA Aerospace Sciences Meething including the New Horizons Forum and Aerospace Exposition*, AIAA 2011-1121. http://dx.doi.org/10.2514/6.2011-1121